

Rowan University

Rowan Digital Works

---

Theses and Dissertations

---

8-5-2021

## Protein-Based Nanofibers and Thin Films for Drug Delivery Applications

Christopher R. Gough  
*Rowan University*

Follow this and additional works at: <https://rdw.rowan.edu/etd>



Part of the [Pharmacy and Pharmaceutical Sciences Commons](#)

---

### Recommended Citation

Gough, Christopher R., "Protein-Based Nanofibers and Thin Films for Drug Delivery Applications" (2021).  
*Theses and Dissertations*. 2935.  
<https://rdw.rowan.edu/etd/2935>

This Thesis is brought to you for free and open access by Rowan Digital Works. It has been accepted for inclusion in Theses and Dissertations by an authorized administrator of Rowan Digital Works. For more information, please contact [graduateresearch@rowan.edu](mailto:graduateresearch@rowan.edu).

**PROTEIN-BASED NANOFIBERS AND THIN FILMS FOR DRUG DELIVERY  
APPLICATIONS**

by

Christopher R. Gough

A Thesis

Submitted to the  
Department of Chemistry and Biochemistry  
College of Science and Mathematics  
In partial fulfillment of the requirement  
For the degree of  
Master of Science in Pharmaceutical Sciences  
at  
Rowan University  
July 28, 2021

Thesis Chair: Xiao Hu, Ph.D.

Committee Members:  
Ping Lu, Ph.D.  
Kandam Ramanujachary, Ph.D.  
Sebastián Vega, Ph.D.  
Samuel Lofland, Ph.D.

© 2021 Christopher R. Gough

## Acknowledgments

I would like to begin by thanking my family and my teachers for their support. They constantly filled me with scientific curiosity and wonder while growing up, leading me to create my own experiments even as a child and help build the scientific mind I have today. Despite no one in my family ever being a scientist or an engineer, they were still immensely helpful to shaping me into the scientist I am today.

I also extend many thanks to all of my friends who I either met at college or followed me through it. Your support and our fun times helped me stay positive through mountains of stress to get me through my degrees. By extension, thank you to everyone who worked alongside me in the lab. Extra special thanks go to my girlfriend, who was always the first one to notice my stress and made sure I took care of myself whenever I fell the hardest.

In the academic setting, I'm thankful to all my professors for inspiring me and giving me insight to cutting-edge research and medicine. There were several opportunities to learn, analyze data, and share with the rest of the scientific community through publications and conferences; these were great helps to my professional development. I especially thank my Chairman Dr. Xiao Hu for all of his guidance, his gratitude, and his companionship for the past four years. Similarly, I thank all my committee members for their help. Thank you to Profs. Lofland, Vega, Lu, and Chary. I am also thankful to Dr. Xiaoyang Mou for his collaboration on cell studies. Finally, thank you to Ted Scabarozzi for his assistance with setting up and maintaining our equipment.

## Abstract

Christopher R. Gough  
PROTEIN-BASED NANOFIBERS AND THIN FILMS FOR DRUG DELIVERY  
APPLICATIONS  
2020-2021  
Xiao Hu, Ph.D.  
Master of Science in Pharmaceutical Sciences

Corn zein and silk are both widely available, easy to extract proteins making them valuable replacements for synthetics. Zein and silk are also promising biomaterials in several applications. This work explores the use of both proteins as drug delivery vehicles by loading 1-Dimensional micro-nanofibers and 2-Dimensional thin films with model drugs or the topical therapeutic sodium citrate. Using a formic acid solvent, powdered zein protein or silk fibers were dissolved into solution and then casted into 2D films or spun into 1D fibers through air-spraying. During dissolution, therapeutic products are added. SEM images showed that fibers maintain their small diameter and porous network at lower amounts of therapeutics. Structural characterization showed that therapeutics could interact and influence secondary protein structure in porous fibers, but not flat films. This interaction improves the thermal integrity of most samples and allowed for greater control of the release of therapeutics from the biomaterial. In summary, the geometry of the biomaterials played an important role in allowing biophysical and biochemical interactions between the therapeutics and the protein structure of the biomaterials. By understanding these interactions, there is more control over material properties and release kinetics. Meanwhile, the fabrication process showed no hindrance on the biocompatibility of the biomaterials in a human cell line.

## Table of Contents

Abstract .....	iv
List of Figures .....	ix
List of Tables .....	xi
Chapter 1: Introduction .....	1
1.1 Biopolymers Within the Scope of Biomedical Applications .....	1
1.1.1 Silk .....	4
1.1.2 Corn Zein .....	4
1.1.3 Casein.....	5
1.1.4 Soy Proteins .....	6
1.1.5 Keratin.....	6
1.1.6 Collagen .....	7
1.1.7 Elastin .....	8
1.1.8 Reflectin.....	9
1.1.9 Composite Materials .....	9
1.2 Project Motivation and Overview .....	10
Chapter 2: Zein-Based Thin Films and Air-Spun Nanofibers for the Topical Delivery of Sodium Citrate .....	12

## Table of Contents (Continued)

2.1 Introduction.....	12
2.2 Materials and Methods.....	15
2.2.1 Preparation of Materials.....	15
2.2.2 Corn Zein Nanofibers .....	15
2.2.3 Corn Zein Films .....	16
2.2.4 Scanning Electron Microscopy (SEM) .....	16
2.2.5 Fourier Transform Infrared Spectroscopy (FTIR) .....	16
2.2.6 Differential Scanning Calorimetry (DSC) .....	17
2.2.7 Thermal Gravimetric Analysis (TGA).....	17
2.2.8 Drug Release Study.....	17
2.2.9 Statistical Analysis.....	18
2.2.10 Biocompatibility Study .....	19
2.3 Results and Discussion .....	19
2.3.1 Structural Characterization .....	19
2.3.2 Thermal Analysis by DSC .....	23
2.3.3 Thermal Gravimetric Analysis (TGA).....	27

## Table of Contents (Continued)

2.3.4 Morphology Analysis.....	30
2.3.5 Drug Release Profile .....	31
2.3.6 Cell Compatibility and Effect of Sodium Citrate Release .....	35
2.3.7 Mechanism.....	40
2.4 Conclusions.....	42
Chapter 3: Study of Silk-Based Thin Films and Air-Spun Nanofibers for Topical Drug Delivery Using Various Model Drugs .....	44
3.1 Introduction.....	44
3.2 Materials and Methods.....	46
3.2.1 Material Preparation.....	46
3.2.2 Silk Nanofibers .....	47
3.2.3 Silk Films.....	51
3.2.4 Morphology Characterization .....	51
3.2.5 Fourier Transform Infrared Spectroscopy (FTIR).....	51
3.2.6 Differential Scanning Calorimetry (DSC).....	52
3.2.7 Thermal Gravimetric Analysis (TGA).....	52
3.2.8 Drug Release Study.....	53



## Table of Contents (Continued)

3.3. Results and Discussion .....	54
3.3.1 Structural Characterization .....	54
3.3.2 Thermal Analysis .....	61
3.3.3 Morphology Discussion .....	75
3.3.4 Drug Release Testing .....	77
3.3.5 Mechanism of Interaction .....	82
3.4 Conclusions .....	85
Chapter 4: Conclusion .....	86
References .....	89

## List of Figures

Figure	Page
Figure 1.1. Preparation of Corn Zein and Bombyx Mori (B. Mori) Silk Solutions.....	3
Figure 2.1. FTIR Absorbance Spectra for Corn Zein Nanofibers.....	20
Figure 2.2. FTIR Absorbance Spectra for Corn Zein Films .....	22
Figure 2.3. DSC Thermograms of Sodium Citrate-Zein Nanofibers.....	24
Figure 2.4. DSC Thermograms of Sodium Citrate-Zein Films .....	26
Figure 2.5. TGA Thermograms of Sodium Citrate-Zein Nanofibers .....	28
Figure 2.6. TGA Thermograms of Sodium Citrate-Zein Films .....	29
Figure 2.7. SEM Images of Sodium Citrate Embedded Zein Nanofibers .....	31
Figure 2.8. Release Profiles of Sodium Citrate from Corn Zein Nanofibers and Thin Films .....	32
Figure 2.9 Light Microscopy of HEK293 Cells on Zein-Citrate Fibrous Mats.....	36
Figure 2.10. MTT Assay of 72-h HEK293 Cell Culture on Zein-Citrate Fibrous Mats.....	38
Figure 2.11. FTIR Analysis on Zein Nanofibers after Citrate Release.....	40
Figure 2.12. Mechanism of Interaction.....	42
Figure 3.1. Silk Biomaterial Synthesis .....	48
Figure 3.2. FTIR Spectra of Silk Fibers.....	57

## List of Figures (Continued)

Figure	Page
Figure 3.3. FTIR Spectra of Silk Films.....	60
Figure 3.4. TGA Thermograms of Silk-Model Drug Fibers.....	63
Figure 3.5. TGA Thermograms of Silk-Model Drug Films.....	66
Figure 3.6. DSC Total Heat Flow Thermograms of Silk-Model Drug Fibers and Films .....	69
Figure 3.7. DSC Reversing Heat Capacity Thermograms of Silk-Model Drug Fibers and Films .....	72
Figure 3.8. SEM Images of Silk-Model Drug Fibers.....	76
Figure 3.9. SEM Images of Silk-Model Drug Thin Films.....	77
Figure 3.10. Release Profiles from Silk-Model Drug Fibers and Films .....	81
Figure 3.11. Mechanism of Interaction.....	84

## List of Tables

Table	Page
Table 2.1. Critical Temperatures Extracted from DSC Analysis on Sodium Citrate Embedded Corn Zein Nanofibers .....	25
Table 2.2. Statistical Comparison of Citrate Release from Zein Nanofibers and Thin Films .....	35
Table 3.1. Physicochemical Properties of Model Drugs.....	50
Table 3.2. Key Temperatures from Thermal Analysis of Silk-Model Drug Fibers and Films .....	73
Table 3.3. Statistical Values from Model Drug Release .....	82

## Chapter 1

### Introduction

#### 1.1 Biopolymers Within the Scope of Biomedical Applications

Biopolymers from nature, especially proteins and polysaccharides, have gained interest in recent times due to their abundance, low cost, biocompatibility, and tunable morphological and physical properties<sup>1-5</sup>. These biopolymers have been used for the development of membranes and nanofibers for biomedical applications including tissue engineering scaffolds<sup>6,7</sup> and for drug delivery<sup>8</sup>. Biopolymers are extremely versatile; silks have extremely high tensile strength while maintaining high elasticity and chitin is used for structural integrity and protection in several insects, for examples. To adapt these materials for biomedical applications, however, several methodologies are used to tune the physiochemical properties of these materials to suit specific applications.

Natural proteins and polysaccharides are relatively inexpensive to regenerate into more useful forms. While this economic advantage is already attractive, the main advantage of biopolymers is their inherent biodegradability and biocompatibility. A critical parameter for the success of drug delivery and tissue engineering applications is minimizing adverse reactions from the host immune response. Through natural enzymes found in the body, biopolymers are degradable and there is little accumulation of toxic by-products<sup>9,10</sup>.

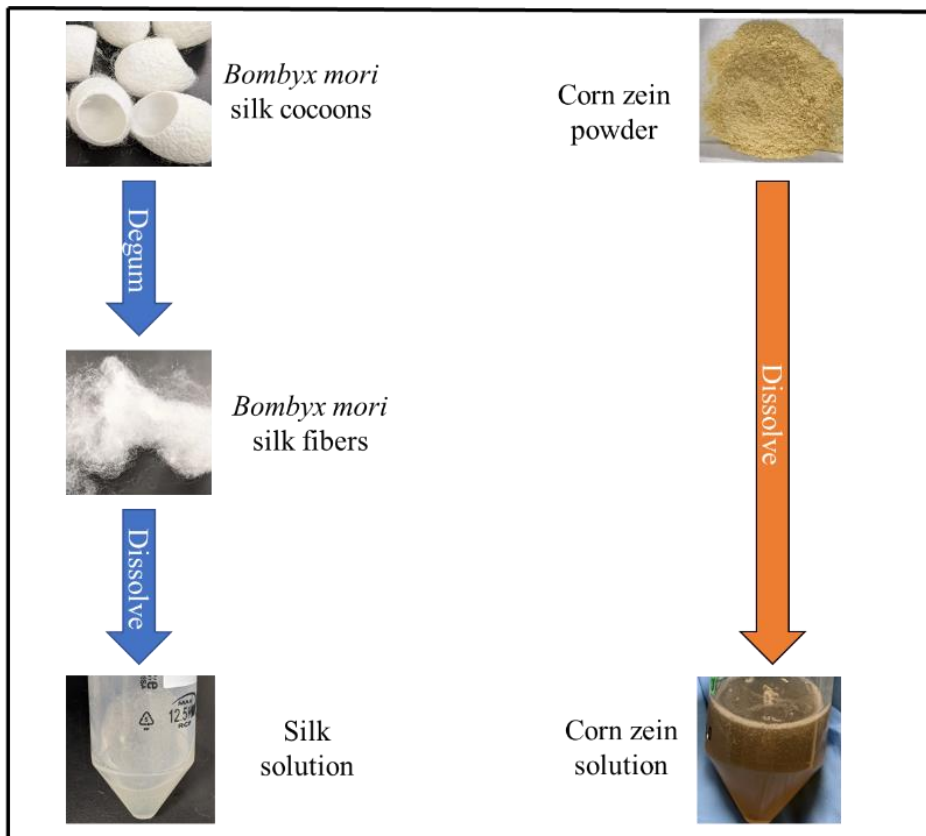
Fibrous materials, especially nanofibers, are becoming increasingly utilized in biomedical research due to their high surface-area-to-volume ratio, mechanical strength, porosity and tunability. Because of the ease of working with natural biopolymers and their biocompatibility and biodegradability, they are an attractive source for nanofiber fabrication. Natural enzymes, some *in vivo*, can degrade fibers into nontoxic metabolites that are reabsorbed by the body. Natural biopolymers can even improve select applications, such as enhancing cell attachment to tissue engineering scaffolds and increase cell proliferation due to native cell attachment motifs <sup>11, 12</sup>. The ease and practicality of natural biopolymers give them appeal in medical applications. Despite these advantages, biopolymer-based fibers remain inferior to many synthetic polymers in their mechanical properties. To improve these properties, natural biopolymer-based fibers can be further modified by crosslinking, blending with other polymers, or additives to form a tunable material. The practicality of each of these methods is highly dependable on the type of manufacturing method used to make the fibers.

While both proteins and polysaccharides are useful natural biopolymers, the original research presented in this thesis focuses purely on protein materials, namely corn zein and *Bombyx mori* (*B. mori*) silk. In present literature, several distinct kinds of proteins and are used, including composite mixtures of proteins. Figure 1.1 illustrates these proteins and any workup required prior to dissolving them into solutions for biomaterial fabrication. The choice of protein varies with the desired material properties of the final biomaterial. Proteins are composed of amino acids, which form long chains of peptides to create the protein's primary structure. Beyond that, various interactions with

itself, other proteins, or the environment including hydrogen bonding, disulfide bonding, London dispersion forces, charge-charge interactions, and dipole interactions shape the primary protein chain into higher-order structures like coils, helices, and sheets. Part of the analysis done in this work examines the role of protein structure for drug delivery carriers.

**Figure 1.1**

*Preparation of Corn Zein and Bombyx Mori (B. Mori) Silk Solutions*



*Note. B. Mori silk cocoons must be degummed by removing sericin prior to dissolution.*

### ***1.1.1 Silk***

Silk proteins are fibrous materials created by various arthropod species by spinning. The natural structure of these fibers is semi-crystalline, containing an ordered structure within a nebulous matrix<sup>13</sup>. The protein structure of these silks varies greatly depending on the species of arthropod producing them; there are at present five different structures that have been identified. These structures include coiled coil, extended beta sheet, cross-beta sheet, collagen-like triple helix and polyglycine II<sup>14-16</sup>. These differences are due to unique, specific amino acid sequences in the protein. As a result, various silks have various material properties including different mechanical strength, thermal integrity, bioactivity, chemical activity, and miscibility with other proteins. This versatility has been utilized to create several silk materials as thin protein films<sup>17-19</sup> and nanofibers<sup>20-22</sup> for a wide range of applications including targeted drug<sup>23</sup> and cytokine delivery<sup>12</sup>, tissue engineering<sup>20, 24, 25</sup>, and soft electronics<sup>26-28</sup>. The mechanical strength of silk has led to its long history in the textile industry, but recently the use of novel solvents<sup>29,30</sup> and treatments<sup>31,32</sup> have been utilized to tailor the beta sheet content of silk fibers in order to fine-tune its mechanical strength for a range of applications.

### ***1.1.2 Corn Zein***

Corn contains several proteins; zein is one of the major storage proteins, which makes it a very abundant source for biomaterials. Much of this comes from the bioethanol industry, where zein is a coproduct. In addition to its abundance, zein is also easily and cheaply extracted<sup>33</sup>. Several different forms of corn zein exist in nature,



including alpha, beta, gamma, and delta zein<sup>34</sup>. Similarly to silk, the properties of zein depend on nanoscale structures and amino acid compositions<sup>35</sup>. Studies have shown that zein is mostly composed of an alpha helical structure<sup>35</sup>, but treatments and fabrication techniques can result in shifts in structure to random coils<sup>8,36</sup> or beta sheets<sup>37,38</sup>. Zein also exhibits good biocompatibility, making it a promising candidate for biomaterials. In current research, zein is frequently used in tissue engineering<sup>39,40</sup> and drug delivery<sup>41</sup>. Zein can also be chemically modified to improve its mechanical properties<sup>42</sup>, which helps overcome its limitations as its films tend to be brittle. Zein can also be turned into fibrous materials since it is thermally and chemically stable during the fiber spinning process; it produces the strongest fibers among vegetable proteins<sup>43</sup>.

### ***1.1.3 Casein***

Casein is a protein comprising roughly 80% of mammalian milk and is easily extracted, making it another widely available protein<sup>44</sup>. It is a glycoprotein that forms two disulfide bridges which help give casein a flexible external structure, as opposed to the set conformations that most proteins have<sup>44</sup>. Because of this, casein tends to organize itself as micelles. In addition to a majority basic amino acid composition, casein also consists of four protein fractions- alpha 1, alpha 2, beta, and kappa<sup>44</sup>, that contribute to its overall material properties. Casein is nontoxic and highly stable, which makes it a promising protein for use in biomaterials including drug delivery<sup>45</sup> and tissue engineering<sup>46</sup>. From a biomedical perspective, casein is not a good candidate for fibrous

materials since it tends to form weak fibers <sup>47</sup>, which makes it difficult to use in conventional methods in the literature such as electrospinning or solution spraying.

#### ***1.1.4 Soy Proteins***

Soy extracts are another attractive protein for material applications. These are globular proteins which consist of two main units, conglycinin 7S and glycinin 11S. Both units are composed of primarily a random coil structure and contain subproteins of varying molecular weights. These units are either water-soluble albumins or globulins soluble in salt solutions, although most soy proteins are globulins <sup>48</sup>. Soy protein isolates are attractive for functional biomaterials because they contain several functional groups that can interact with the surrounding environment. To date, soy proteins have been used for pollutant filtering <sup>49</sup>, adhesives <sup>48</sup>, and oxidation inhibition <sup>50</sup>. Biomaterials is another major area of research for soy proteins, including tissue engineering <sup>51,52</sup> and microencapsulation <sup>53</sup>. The biggest downfall of soy-based materials is a lack of mechanical strength, which is often solved by creating soy composites with other polymers. This lack of mechanical strength is also the reason soy fiber materials are not possible without the addition of other polymers.

#### ***1.1.5 Keratin***

Keratin, which is extracted from wool fibers, is another naturally derived protein commonly used for biomedical applications. Wool fiber keratin is often processed into nanofibers for various applications <sup>54,55</sup>, but other sources of keratin can provide keratin with different overall material properties. These other sources include horns, fingernails,

hair, and feathers. This results in several different types of keratin available in nature due to amino acid substitutions. For example a severe skin disease results from a substitution of methionine amino acid with threonine in keratin 14 because a hydrophobic, nonpolar amino acid is substituted with a hydrophilic, polar amino acid <sup>56</sup>. This disease damages the structural integrity of keratin that makes up the stratum corneum of the skin, highlighting how the integrity of keratin biomaterials is also heavily affected by amino acid sequences. This also applies to filtration applications, where natural keratin is used for the absorption of heavy metal ions due to its high amount of polar amino acids <sup>55</sup>. The structure of keratin is distinct from other proteins in that it contains a high number of cysteine residues that form inter- and intra-molecular disulfide bonds, creating a compact 3D structure that is resistant to chemicals <sup>57</sup>. Keratin structure can further be distinguished into alpha and beta keratins. Alpha keratin, also called hard keratin, found in hair, wool, and nails, contains a higher sulfur content and consists of fibrils made up of intermediate filaments. Beta keratin, meanwhile, has a lower sulfur content and is found in birds, reptiles, and the stratum corneum of skin <sup>57</sup>. The biocompatibility and strength of keratin make it a widely used natural biopolymer in biomedical research, including in tissue engineering <sup>58,59</sup> and drug delivery <sup>60</sup>, often using films or fibrous materials.

### ***1.1.6 Collagen***

Collagen is naturally found in over 29 different types. Its triplicate amino acid sequence enables collagen to form stable triple helices which can further develop into quaternary structures, giving rise to mechanically strong fibrils such as collagen V and XI

<sup>61</sup>. Collagen I, II, and III are also common fibril structures in the body, but every type of collagen provides unique signaling abilities *in vivo* for biomaterial applications <sup>62</sup>.

Dissolution of collagen partially destroys the triple helical structure, but allows it to regenerate into nanofibers <sup>63</sup>. Nanofibers, films, and hydrogels are the most common biomaterials made from collagen, and collagen I is mainly used due to its abundance in nature <sup>61</sup>.

### ***1.1.7 Elastin***

Another biomaterial protein that is a common native protein *in vivo* is elastin. Elastin is a critical protein component of the extracellular matrix (ECM) that provides elasticity in tissues and organs. It pairs with collagen, where collagen provides structure and mechanical strength, while elastin provides flexibility. Elastin is especially important in the lungs, aorta, and skin, where elasticity is crucial <sup>64</sup>. Once again, amino acids play an important role in the structure and function of elastin just as with the other proteins discussed. By oxidizing lysine residues, elastin molecules uncoil to bind and crosslink other proteins and form elongated chains <sup>65</sup>. Because of its elasticity and relationship to the ECM, elastin is a common protein used for vascular tissue engineering and blood-interfacing biomaterials <sup>66</sup>. Elastin is also used in other areas of tissue engineering including as a skin substitute <sup>67</sup>. Most scaffolds using elastin, however, are combined with a material that is stronger mechanically like collagen. A popular topic in current research for elastin is self-folding proteins, where research has studied elastin's self-assembly into fibers, hydrogels, sheets, and more <sup>68-72</sup>.

### ***1.1.8 Reflectin***

First reported in 2004, reflectins are a relatively new class of proteins with unique spectral and optical properties, which allow self-assembly into reflecting materials <sup>73</sup>. These proteins are found naturally in animals such as cephalopods and squids which use the special optical properties of reflectin for camouflage. A wide dynamic of structural colors is possible using reflectins due to a hierarchy of assembly at the nanoscale level <sup>74</sup>. Current research into understanding this assembly hopes to design biomaterials with complex optical functions like active camouflage or contact lenses. Within conventional tissue engineering, reflectin has been used for neural tissue engineering to promote stem cell differentiation <sup>75</sup>. Reflectin, too, is able to be processed into fibers through dissolution in organic solvents like conventional proteins <sup>76</sup>.

### ***1.1.9 Composite Materials***

Most structural materials in biological systems are composites of biomacromolecules arranged in some hierarchy. The exoskeleton of arthropods, for example, is a dispersion of chitin within a matrix of silk-like proteins. Attempts to mimic this hierarchy behavior in biomaterials has shown that the physicochemical and morphological properties of the composite biomaterial (biocomposite) can be altered using natural materials such as silk, cellulose, and chitosan, or as a function of the fabrication method <sup>77-79</sup>. Despite this research, it is still unclear how the hierarchy of biocomposite self-assembly dictates the secondary structures formed during biomaterial fabrication. Being able to predict the relationship between these hierarchies and the

overall physicochemical properties of a biomaterial would be a powerful tool. Along with this understanding, manipulating molecules to form structures with targeted size, spacing, and shape can create rapid fabrication of complex multi-level structures from a single biocomposite fabrication. Some biomaterials research has shown beta-sheet crystallites provide a network for crosslinking proteins to enhance their mechanical properties, but the morphology of the biomaterial is dependent on fabrication conditions and post-fabrication treatments<sup>80, 81</sup>. Understanding the mechanisms of molecular self-assembly will be essential to defining the natural nanoscale hierarchies that form powerful biocomposites in nature, and allow for the creation of powerful, fine-tuned biomaterials for a wide variety of applications.

## **1.2 Project Motivation and Overview**

All the above materials (biopolymers) are excellent candidates for drug delivery applications due to their biocompatibility, biodegradability, and tunable surface properties. Protein-based materials have long been an attractive alternative to synthetic materials for the production of plastic films<sup>19, 42, 82-91</sup> and fibers<sup>8, 22, 30, 36, 43, 55, 82, 92-110</sup> due to the availability of proteins, their ease of processing, and the tunability of protein-based material properties. The success of proteins used as drug delivery vehicles is a large part in this project's motivation.<sup>8, 23, 36, 41, 51, 60, 70, 96, 111</sup>. We envision that proteins provide a cheap, easy, and biocompatible platform for a topical drug patch with tunable material properties to cater to a wide range of application sites and therapeutics. In addition, the substructures of proteins and the functional groups along their backbones provide an

additional means of controlling the release of therapeutics from the patch.<sup>8, 10, 36, 51, 70, 111,</sup>

112

Today, drug delivery still faces several challenges from the patient level to the manufacturing level. For one, synthetic polymers are typically formed from petroleum byproducts or with harsh solvents that can harm the ecosystem. Even after production, most synthetic polymers are nonbiodegradable, which contributes to pollution after the product's use. Biopolymers can be fabricated with less volatile solvents, some even recyclable,<sup>113</sup> and are biodegradable products themselves, which helps combat pollution. Recycling and biodegradability make them more economic than synthetic polymers, which require constant replenishing and complicate disposal methods.

From the perspective of patients and healthcare professionals, drug delivery is also challenging. Patient compliance- ensuring patients take their intended dosage at the correct intervals- can be difficult. Therefore, this study tries to envision a simple patch that can be fine-tuned to control the release of various therapeutics at various rates. This patch would also reduce off-target effects. While topical drugs are applied to a local area on the skin, they still face issues from off-target effects from how far the therapeutic penetrates into the skin or staining of clothes that can be improved by incorporating them into a delivery vehicle.<sup>114</sup> The protein-based patches developed in this study effectively integrate with the therapeutic molecules being delivered to improve the efficacy of their delivery to patients.

## Chapter 2

### Zein-Based Thin Films and Air-Spun Nanofibers for the Topical Delivery of Sodium Citrate

#### 2.1 Introduction

One of several complications of diabetes is ulcers on the foot. If left untreated, these wounds can lead to infections that lead to further complications, morbidity, or amputations.<sup>115, 116</sup> While several treatment options exist, they only offer relief to a fraction of patients and come with undesired side effects.<sup>117</sup> An alternative treatment that minimizes side effects and improves patient compliance utilizes citrus flavonoids delivered through a wound dressing.<sup>118</sup> One such flavonoid, utilized in this study, is sodium citrate. Flavonoids promote healing through their anti-inflammatory, antioxidant, antiatherogenic, hepatoprotective, and neuroprotective properties. Citrate is often used in drug delivery applications due to its ability to curate the immune response.<sup>119-121</sup> In diabetic specifically, sodium citrate helps correct magnesium deficiency through its chelating properties.<sup>122</sup>

The topical delivery of citrus flavonoids provides many benefits over other delivery routes including lower dose requirements and minimized off-target effects. Several different vehicles have been explored for drug delivery including micelles<sup>123, 124</sup>, liposomes<sup>125, 126</sup>, nanoparticles<sup>127, 128</sup>, nanofibers<sup>129</sup>, and thin films<sup>130</sup>. The use of these different vehicles allows for controlled, long-term release of topical drugs when placed on the skin to increase the efficacy of the treatment and the compliance of the patient.



Nanofibers and thin films in particular are typically easy to manufacture on a large scale, but maintain their specific targeting which improves efficacy and eliminates side effects<sup>130</sup>. Thin films create a bioavailable platform for rapid drug release, allow a fast onset of action and reducing the frequency of doses<sup>130</sup>. Nanofibers have also shown high promise for dermatological drug delivery due to their strong mechanical properties, low density, high porosity, and large surface area to volume ratio which provides a platform for enhanced drug loading<sup>131</sup>.

Corn zein is a widely available protein, comprising roughly 80% of the total protein content found in corn and being a byproduct of bioethanol refinement<sup>93, 132-138</sup>. In biomedical and pharmaceutical applications, corn zein has been widely used by itself and in composite materials with some of the most successful applications using fiber and thin film materials<sup>139, 140</sup>. Much of the success of corn zein can be attributed to its good biocompatibility and biodegradability. These properties have resulted in its use in several topical drug delivery applications<sup>34, 111</sup>. Corn zein-based biomaterials also show antioxidative activity, which assists in wound healing and prevents damage to cells near the site of application<sup>141, 142</sup>.

Biomaterials made from corn zein or composites of corn zein are flexible with high tensile strength, making them ideal for films<sup>11, 83, 143-145</sup>, nanofibers<sup>95</sup>, and composites<sup>146</sup>. Fabrication of nanofibers in particular is easy because zein is hydrophobic and insoluble in water. While electrospinning is one of the most common methods for nanofiber fabrication in current literature, it requires a high voltage source which limits

the overall efficiency of the process due to energy demands and dielectric constants<sup>147</sup>. To avoid these problems, air-jet spinning, also known as solution spraying, as utilized in this study. Air spinning utilizes compressed air and a concentric nozzle to stretch a polymer solution into fibers through high shear forces which cause the solvent to evaporate off, leaving behind polymer nanofibers that are deposited onto a collection surface<sup>148-150</sup>. This method of production is economical, simple to reproduce, and easily scales up to produce a large volume of nanofibers from polymer solutions with high efficiency.

Within this study, corn zein was used to fabricate nanofibers and thin films incorporated with sodium citrate at different concentrations (1-30% wt drug/wt zein). These composite systems created a method for targeted, controlled delivery of sodium citrate to specific skin targets affected by diabetic ulcers<sup>112, 151, 152</sup>. Material characterization was done using FTIR, DSC, TGA, and SEM to understand the effects of sodium citrate on corn zein nanofibers and films. A cell biocompatibility study was also done to ensure biocompatibility after fabrication and after release of sodium citrate from the materials. Finally, a time-based drug release study quantified the release of sodium citrate from zein nanofibers and thin films and was used to understand the difference between 1D nanofiber geometry and 2D film geometry during drug delivery. The results suggested that nanofibers offer a better vehicle than films, since sodium citrate can interact with the secondary protein structure of zein nanofibers to shift them towards a more stable alpha-helical structure. After the citrate is released, however, the protein structure of zein nanofibers reverts to its original random coil structure. This reversible

transition, controlled transition showcases the potential for corn zein nanofibers to be used for the delivery of other topical drugs.

## **2.2 Materials and Methods**

### ***2.2.1 Preparation of Materials***

All materials obtained from companies were used without further modification. Corn zein powder of purity greater than 87% was obtained as a gift from POET, LLC. ACS Formic of 98% Grade was purchased from EMD Millipore Corporation and used as a solvent. For samples containing drug, sodium citrate tribasic dihydrate with greater than 99% purity for molecular biology from Sigma-Aldrich was used.

### ***2.2.2 Corn Zein Nanofibers***

Corn zein solutions were first created by dissolving 5.3 g of corn zein in 10 mL of formic acid. Homogenization was ensured using a benchtop vortexer. In samples containing 1%, 5%, 10%, 15%, 20%, or 30% (wt drug/wt zein) sodium citrate was dissolved in formic acid prior to adding corn zein. Once fully dissolved and homogeneous, the solutions were transferred to a disposable syringe to attach it to a siphon-feed airbrush. An air compressor provided 100 psi of pressure to the airbrush in order to shear the solution into nanofibers. Nanofibers were collected into an aluminum foil lined box a distance of 1.5 m away from the airbrush. Collected nanofibers were dried in a vacuum oven at 60 °C overnight to evaporate excess formic acid prior to any characterization.

### ***2.2.3 Corn Zein Films***

Corn zein films were also fabricated to compare the effects of 1D nanofiber geometry to 2D thin film geometry for drug delivery applications. The protein solution for films were prepared the same way as the solutions for nanofibers above. Instead of using an airbrush, 2 mL of each sodium citrate-zein solution was casted onto a PDMS mold for each wt% of citrate. Casted solutions dried at room temperature for 2 days, followed by removal of excess formic acid in a vacuum oven at 60 °C overnight. The final thickness of the films measured around 20  $\mu\text{m}$ .

### ***2.2.4 Scanning Electron Microscopy (SEM)***

Scanning Electron Microscopy (SEM) was used to measure the surface morphology of fiber and film samples using a LEO 1530 VP SEM at an EHT of 10 kV. Prior to imaging, samples were sputter coated with gold for 15 s.

### ***2.2.5 Fourier Transform Infrared Spectroscopy (FTIR)***

For further morphology analysis, Fourier Transform Infrared Spectroscopy (FTIR) was performed on samples with a Bruker Tensor 26 Fourier Transform Infrared Spectrometer equipped with deuterated triglycine sulfate detector under nitrogen purge gas at 50 mL/min. Spectra was obtained from 4000 to 400  $\text{cm}^{-1}$  with 64 scans at 4  $\text{cm}^{-1}$  interval resolution using a multiple reflection, horizontal MIRacle ATR attachment. To ensure homogeneity, all samples were measured at least once on both sides. Between samples, the ATR crystal was cleaned with alcohol and 64 background scans were taken.

### ***2.2.6 Differential Scanning Calorimetry (DSC)***

To analyze the thermal stability and miscibility of the composites, temperature modulated differential scanning calorimetry (TM-DSC) was performed using a Q100 DSC outfitted with a refrigerated cooling system (RCS). Before use, the instrument was calibrated against indium standards for heat flow and temperature and with aluminum and sapphire standards for heating capacity. 5 mg of each sample was enclosed into aluminum pans and analyzed from -40 to 400 °C at a heating rate of 20 °C/min, temperature amplitude of 0.318 °C, and modulation period of 60 s. Nitrogen purge gas at 50 mL/min was used to prevent oxidation.

### ***2.2.7 Thermal Gravitational Analysis (TGA)***

Further thermal analysis was performed by thermal gravitational analysis (TGA) using an SDT-Q600 instrument. The mass of samples was recorded over a 25-800 °C range at a constant rate of 10 °C/in while under nitrogen purge gas at 100 mL/min. The starting mass of all samples was 5 mg.

### ***2.2.8 Drug Release Study***

Samples of select citrate concentrations (5%, 10%, 20%, 30% wt drug/wt zein) were prepared in sets of five along with triplicate samples of 0% zein nanofibers. 0% nanofibers were used as error bars to account for mass lost due to fiber degradation; all samples measured about 6 mg. All samples soaked in 200 µL of deionized water over a 72 h time period. At designated times (0.25, 0.5, 1, 2, 3, 4, 5, 6, 12, 24, 36, 48, 60, 72 h)

samples were moved to a new, clean well with 200  $\mu\text{L}$  of deionized water. Parafilm was used to cover the wells between measurement times to prevent contamination or loss of water. To measure the amount of drug released into each water well, the solutions were run through pre-weighed filter paper and then excess water was dried off in a vacuum oven. The filter paper was then re-weighed to record the amount of drug released at that time point. The sum of each of these mass points was recorded to plot a cumulative drug release plot for each set of citrate weight percentage using the average of the five samples. At the end of the study, the remainder of the samples was dried in a fume hood for 4 days and their final mass was recorded.

### ***2.2.9 Statistical Analysis***

To compare the release of citrate between fibers and films, a paired two-sample t-test was performed using Excel. A null hypothesis was proposed that the mean amount of drug released from fibers was the same as the mean amount of drug released from the films. Each pair of samples (fibers and films) for each wt% (1%, 10%, 20%, 30 wt%) was tested separately. 11 time points were recorded, giving the test 10 degrees of freedom. A 5% significance level was chosen, giving a two-tailed alpha level of 0.05. To test for covariance, the Pearson correlation coefficient was also calculated between each wt% group. The T-statistic, T-critical, and p-value for each test was used to determine statistical significance.

### **2.2.10 Biocompatibility Study**

To confirm the biocompatibility of the samples, HEK293 (human embryonic kidney) were grown of samples using Dulbecco's modified Eagle's medium supplemented with 10% fetal bovine serum (FBS) and 100 U/mL Penicillin-Streptomycin. Culturing conditions were in an atmosphere of 95% air and 5% carbon dioxide at 37 °C according to NIH standards. Samples were first sterilized under UV light overnight, then an equal amount of cells were seeded on both fiber mats and thin films. Cells were also seated on a blank petri dish was used as a control. After 72 h of culturing, a 3-[4,5-dimethylthiazole-2-yl]-2,5-diphenyltetrazolium bromide (MTT) assay was used to quantify cell viability.

## **2.3 Results and Discussion**

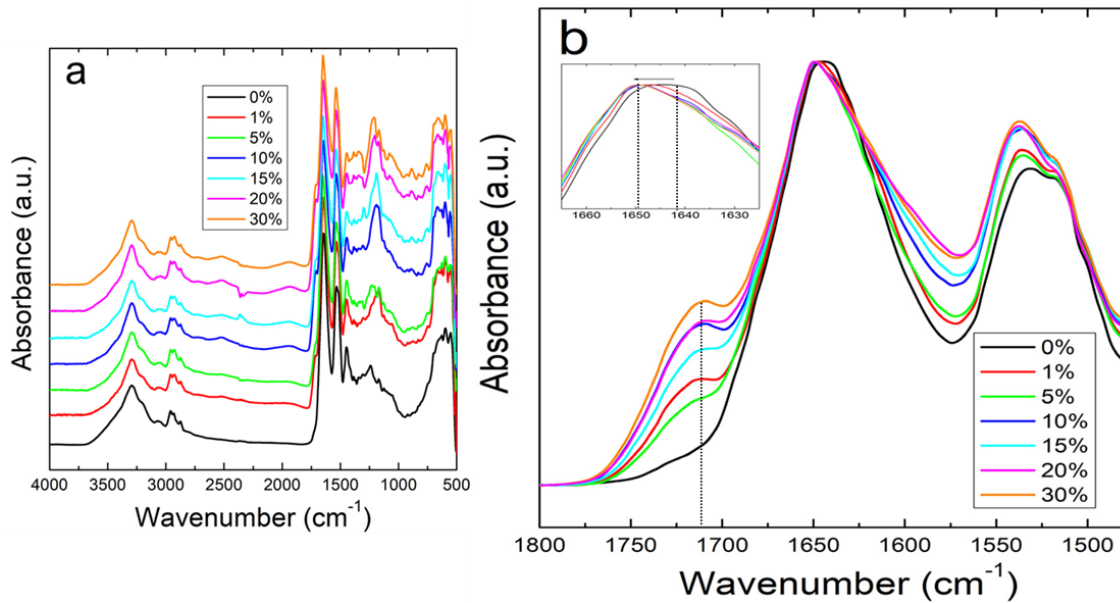
### **2.3.1 Structural Characterization**

To begin understanding the interactions of sodium citrate with the structure of corn zein, FTIR was first used. A comparison was performed between corn zein fibers and thin protein films with varied weight percentages of sodium citrate (0%, 1%, 5%, 10%, 15%, and 30%). The full absorbance spectra of zein fiber samples is showed in Figure 2.1a with Figure 2.1b showcasing the changes in secondary protein structure in the Amide I and II regions. Within the Amide I region, corn zein without any citrate shows an absorption peak at  $1650\text{ cm}^{-1}$  which indicates a random coil network.<sup>153-155</sup> After sodium citrate is added, all embedded samples see a shift in the absorbance peak to  $1650\text{ cm}^{-1}$  which represents an alpha-helical protein structure. This analysis indicates that in

1D fibers, zein protein interacts with sodium citrate through hydrogen bonds or charge-charge interactions to shift the protein from a random coil network towards a more orderly structure. In the Amide II region (Figure 2.1a), this interaction is further supported by shifts in absorbance in the region associate with the protein side chain. Specifically, pure zein shows a peak at  $1531\text{ cm}^{-1}$  which shifts to  $1538\text{ cm}^{-1}$  in citrate-loaded fibers due to the denser alpha helices pushing more zein side chains to become exposed on the protein backbone.

**Figure 2.1**

*FTIR Absorbance Spectra for Corn Zein Nanofibers*



*Note.* (a) Full FTIR spectra. (b) Amide I and II Regions of Fibers. Unloaded fibers show a peak at  $1640\text{ cm}^{-1}$  indicative of random helical structure while fibers loaded with

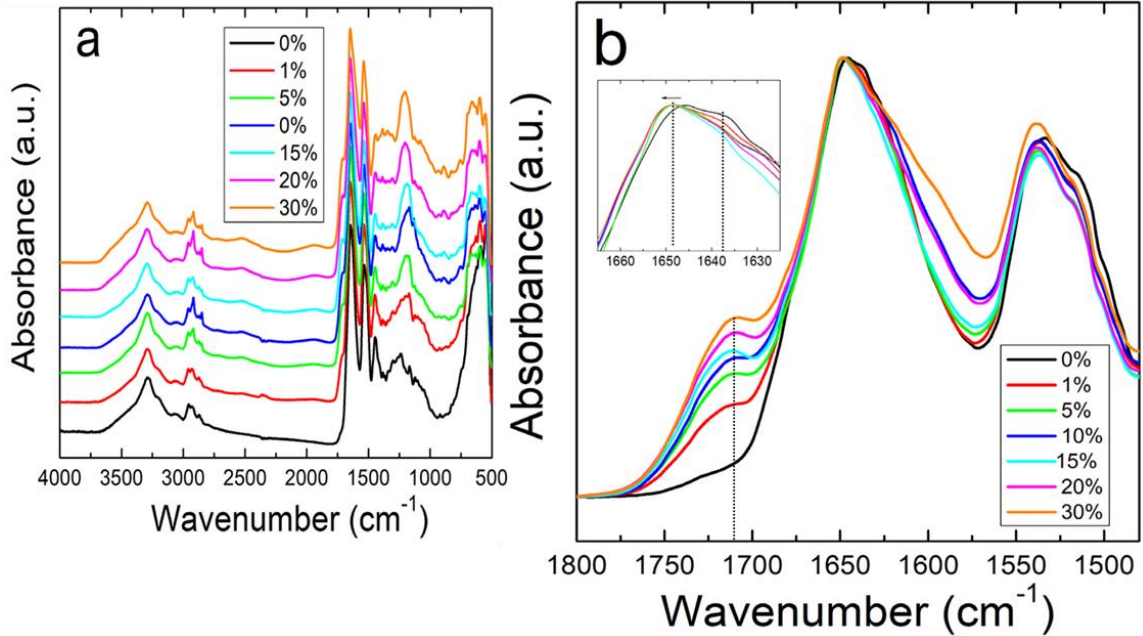


sodium citrate show a shift to alpha helical structure at  $1650\text{ cm}^{-1}$ . All samples with citrate show shoulder at  $1720\text{ cm}^{-1}$  that scales with wt% of citrate.

Thin films do not show the same interaction with sodium citrate that the nanofibers do. The full FTIR spectra of the zein films is shown in Figure 2.2a, with the Amide I and II regions highlighted in Figure 2.2b. Zein films without citrate contain a peak at  $1647\text{ cm}^{-1}$  which indicates an alpha-helix dominated structure<sup>156</sup>. The addition of citrate does not produce any clear trends, but does decrease the shoulder at  $1638\text{ cm}^{-1}$  which corresponds to a decrease in random coil structure. This behavior is also related to zein's inherent tendency to decrease in alpha helical structure after exposure to solvents<sup>38</sup>. Thin films see the introduction of a peak unique to the films at  $1386\text{ cm}^{-1}$  which is often associated with symmetric -COO bond stretching<sup>157</sup>. This peak is likely caused by residual formic acid trapped inside of the 2D films due to the nature of film fabrication. Where residual formic acid is mostly evaporated during nanofiber fabrication because of the shear forces with the remainder removed during drying, film fabrication results in residual acid trapped inside the films during casting.

**Figure 2.2**

*FTIR Absorbance Spectra for Corn Zein Films*



*Note.* (a) Full FTIR spectra. (b) Amide I and II regions for films. Unlike the nanofibers, there is an insignificant shift in absorbance peak when sodium citrate drug is embedded. Like in the fibers, all samples with citrate show shoulder at 1720 cm<sup>-1</sup> that scales with wt% of citrate.

Both fiber and film samples with sodium citrate see a shoulder at 1710 cm<sup>-1</sup> that scales in intensity with an increase in wt% of sodium citrate. Accordingly, fibers and films without sodium citrate lack this peak (Figure 2.1b and Figure 2.2b). All samples also see a shoulder at 1710 cm<sup>-1</sup> as a result of C=O bond stretching caused by hydrogen

bonding between protein side chains and sodium citrate molecules<sup>158</sup>. Further evidence of side chain interactions is also evident in the peak at 1572 cm<sup>-1</sup> in citrate-embedded samples. This argument is made based on previous literature indicating that this peak is caused by asymmetric stretching of -COO bonds<sup>157</sup>. There is also a broad peak in all samples in the 2000-1800 cm<sup>-1</sup> region commonly associated with the presence of water.

### **2.3.2 Thermal Analysis by DSC**

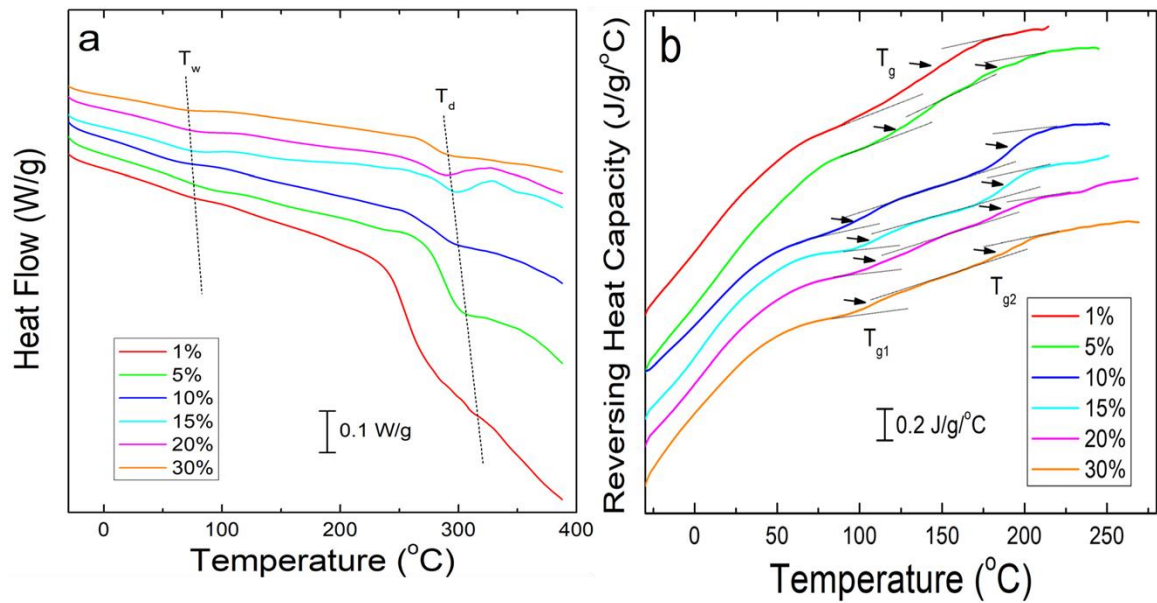
Thermal analysis was first performed using temperature modulated differential scanning calorimetry (TM-DSC) on corn zein nanofibers embedded with sodium citrate. Two key temperatures (Table 2.1) were extracted from all samples based on the thermogram in Figure 2.3a. These are  $T_w$ , related to the evaporation of water embedded in the samples, and  $T_d$ , related to degradation of the bulk samples themselves. All samples are stable well above physiological conditions, rendering them safe for the delivery of various therapeutics and for transportation or storage in hot climates.

TM-DSC was also used to see changes in reversing heat capacity in the samples (Figure 2.3b). The zein-citrate composite fiber samples all showed two glass transition temperatures ( $T_g$ ), although the lower  $T_g$  is much broader at lower wt% of citrate and becomes more defined at higher wt%. This trend indicates that the lower  $T_g$  is related to citrate-zein interactions. The higher  $T_g$  is much more defined in all samples. This, coupled with their correlation to the thermograms produced by thermal gravimetric analysis (TGA), indicate that this  $T_g$  is related to the breakdown of the bulk composite material. Past this higher  $T_g$ , the composites begin to break down (Figure 2.3b). Since the

corn zein-citrate nanofiber composites have a high initial  $T_g$  ( $>100$  °C) and a narrow step in heat capacity, this analysis implies that the nanofibers are ideal drug delivery vehicles for sodium citrate due to strong interactions that form a thermally stable structure.

**Figure 2.3**

*DSC Thermograms of Sodium Citrate-Zein Nanofibers*



*Note.* (a) Heat flow changes at  $T_w$  due to water evaporation and  $T_d$  due to thermal degradation. (b) Step changes in reversing heat capacity can be found at  $T_{g1}$  and  $T_{g2}$  for the fiber samples with the drug. The step at  $T_{g1}$  is much more defined at higher wt% of citrate.

**Table 2.1**

*Critical Temperatures Extracted from DSC Analysis on Sodium Citrate Embedded Corn Zein Nanofibers*

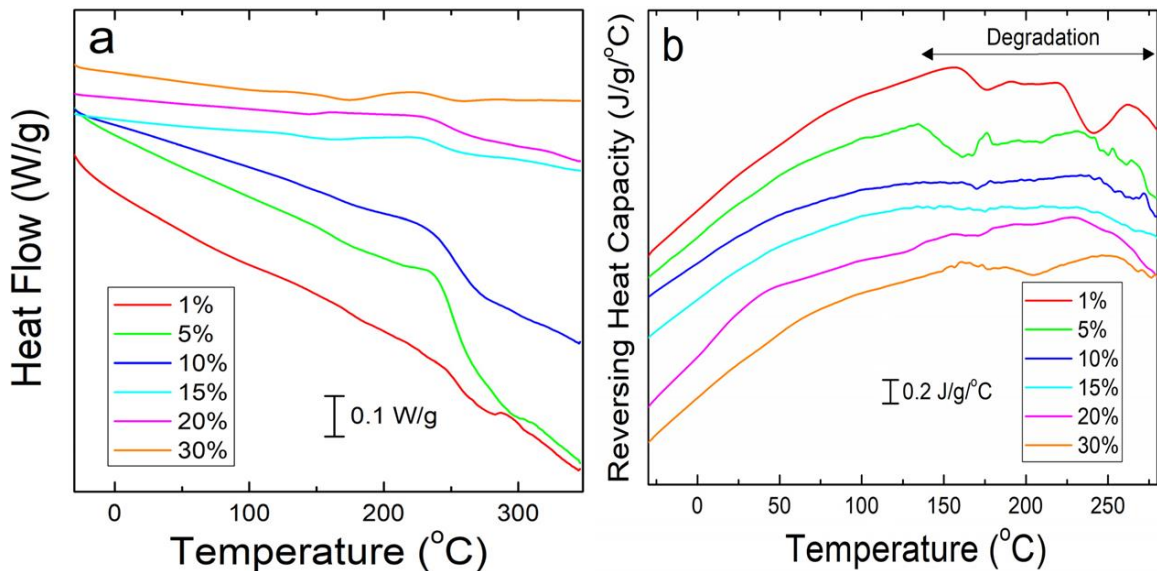
<b>Citrate wt%</b>	<b>T<sub>w</sub> (°C)</b>	<b>T<sub>d</sub> (°C)</b>	<b>T<sub>g1</sub> (°C)</b>	<b>T<sub>g2</sub> (°C)</b>
1	81	311	139	N/A
5	83	305	128	189
10	73	297	104	190
15	78	297	109	188
20	75	290	116	187
30	69	289	105	186

A parallel DSC analysis was also performed on corn zein protein films embedded with sodium citrate. Due to the thermally unstable nature of these composites, there is less numerical data to extract from this analysis. Regardless, a visible trend can still be seen in the thermogram in Figure 2.4a. With higher percentages of citrate, the composite films see less degradation, which implies that sodium citrate still helps to stabilize the thin films despite lacking the strong interactions seen in the nanofiber composites based

on FTIR analysis. This lack of interactions causes all film composite samples to degrade earlier than the nanofiber composites; nanofiber samples do not begin degrading until at least 250 °C, but films show major degradation by 220 °C. Even analyzing the reversing heat capacity (Figure 2.4b) of the film composites, the only trend that can be seen is a reduction in noise with an increase in wt% of sodium citrate. Regardless, all films still begin degradation around 150 °C.

**Figure 2.4**

*DSC Thermograms of Sodium Citrate-Zein Films*



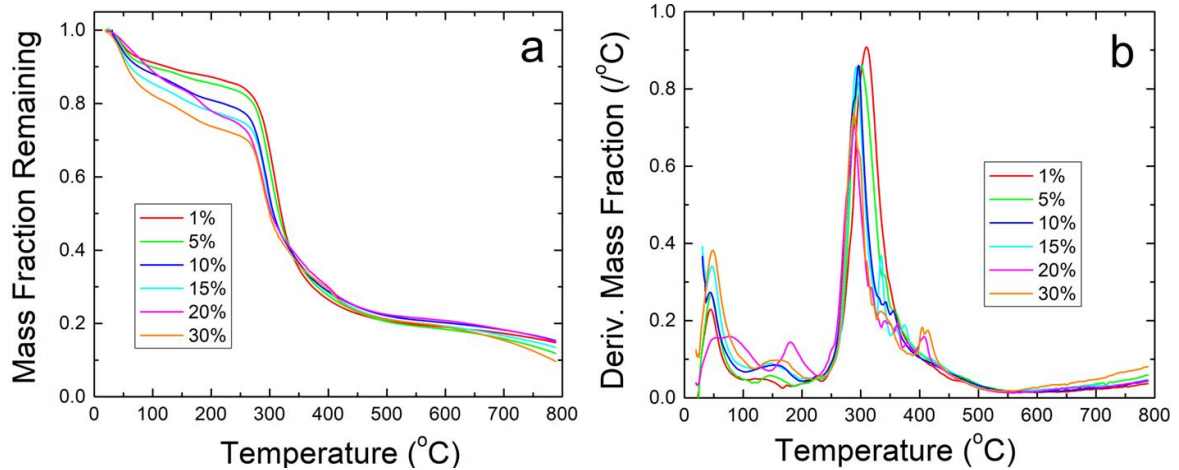
*Note.* (a) Heat flow thermogram of zein-citrate composite films. Degradation begins earlier than in nanofiber composites. (b) Reversing heat capacity thermogram shows noise due to the thermal instability of the composites beginning at 150 °C.

### **2.3.3 Thermal Gravimetric Analysis (TGA)**

The results from DSC analysis were further cross-checked using TGA. Nanofiber composites were first analyzed and compared to the  $T_w$  and  $T_g$  found from DSC. The thermogram produced (Figure 3.5a) shows sharp decreases in sample weight at temperatures corresponding well to the  $T_w$  and  $T_g$  values found during DSC analysis. The derivative of mass loss shown in Figure 3.5b demonstrates the superior thermal stability of the nanofiber composites. The initial change in mass around 50 °C correlates to  $T_w$ . This peak shifts to lower temperatures in samples containing a higher wt% of citrate due to higher bound water content. Most of the mass loss in the samples occurs in the 300-350 °C region, which correlates to the  $T_d$  found during DSC analysis as temperatures approach the degradation temperature of zein protein<sup>156</sup>.

**Figure 2.5**

*TGA Thermograms of Sodium Citrate-Zein Nanofibers*



*Note.* (a) Weight fraction of zein-citrate nanofibers up to 800 °C. (b) First derivative of the remaining mass helps visualize two peaks due to bound water evaporation and zein degradation.

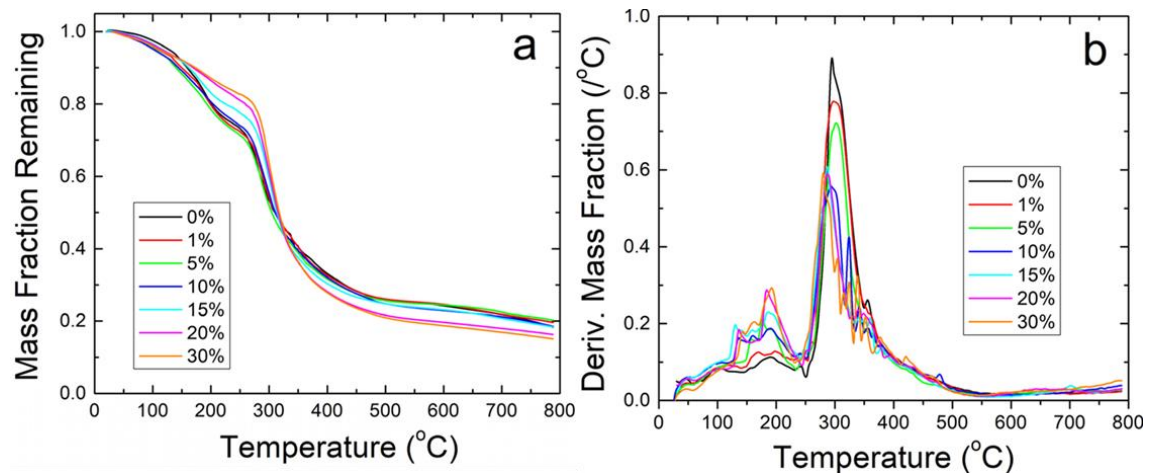
A similar analysis was also performed on corn zein sodium citrate composite films using TGA. Similar to the DSC results, TGA confirmed that film composites are less thermally stable than their nanofiber counterparts. All samples show a large amount of degradation, although samples with higher amounts of citrate resist degradation slightly better (Figure 2.6a). The thermal instability of protein films is further shown through the differential thermogram in Figure 2.6b, where several small peaks are visible between 100-250 °C due to noise. Another parallel to the DSC analysis is the lack of a degradation peak related to water evaporation. There is also good correlation between the



TGA thermogram in Figure 2.4b and the DSC thermogram in 2.6b in that both show major degradation of the zein film composites beginning around 150 °C. The TGA analysis does show that sodium citrate may interact with protein films in some way to help stabilize them at high weight percentages of citrate, but this interaction is not comparable to that in the nanofibers as evident by their lower onset of degradation and the lack of changes in protein structure (FTIR analysis). Thus, despite film composites maintaining a higher weight percentage overall, nanofiber composites still hold stronger thermal integrity over a higher temperature range.

**Figure 2.6**

*TGA Thermograms of Sodium Citrate-Zein Films*



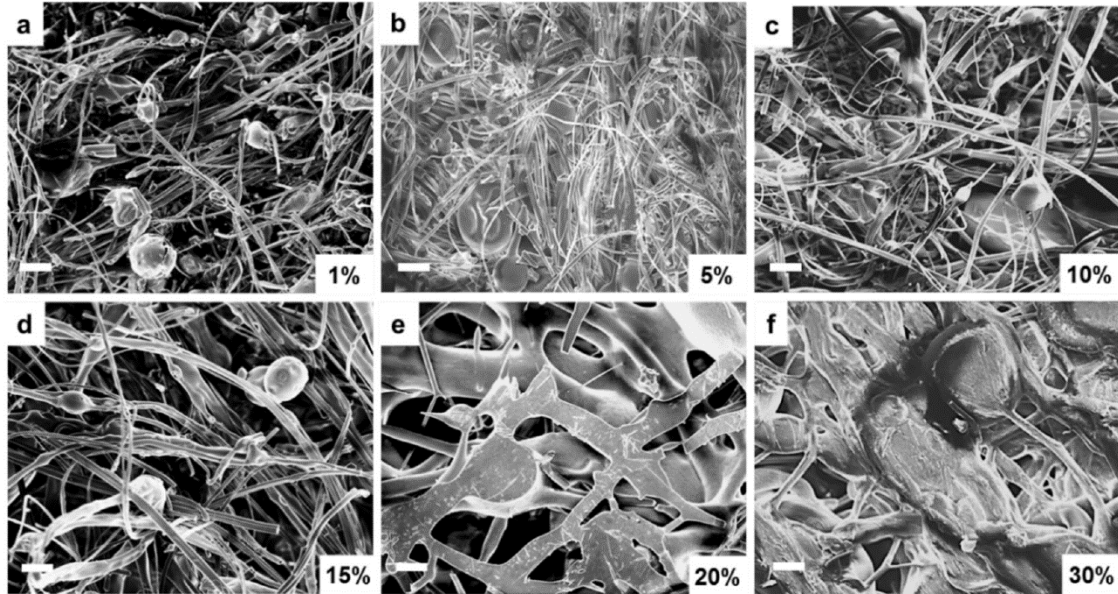
*Note.* Weight fraction of zein-citrate films up to 800 °C. Samples retain a higher mass overall but degrade much earlier than nanofibers. (b) First derivative of the remaining mass. The large presence of noise indicates thermal instability.

### **2.3.4 Morphology Analysis**

Given the results of the structural and thermal analysis given above, it was decided that corn zein film composites were not suitable for long-term biomedical applications. Because of this, the remainder of this study focused exclusively on the use of nanofibers for biomedical applications including drug delivery. Scanning electron microscopy (SEM) was performed on several nanofiber samples of varying wt% of embedded citrate to study its effects on the nanofiber mesh morphology. The results showed that at lower wt% of citrate ( $\geq 10\%$ ), the composite samples can maintain their desirable nanofiber properties (Figure 2.7a-c). Specifically, the nanofibers maintain nanoscale diameters and the fiber network stays porous, which allows for cell infiltration and the transport of embedded drugs. The nanofibers also maintain a high surface area-to-volume ratio, which benefits many applications of fibrous materials<sup>8, 96, 129, 131, 159, 160</sup>. Some small droplets of sodium citrate are still visible in these images, but the overall morphology of the nanofiber network is mostly unaffected. When compared to higher wt% of sodium citrate (15-30 wt%) (Figure 2.7d-f) the fibers become saturated with citrate and form large globules that deteriorate the benefits of a nanofibrous mat. In these samples, the fibers lose their nanoscale diameters and the globules of citrate cause the fiber network to lose most of its porosity.

**Figure 2.7**

*SEM Images of Sodium Citrate Embedded Zein Nanofibers*



*Note.* Sodium citrate varies from 1 to 30 wt% citrate/zein: (a) 1 wt%, (b) 5 wt%, (c) 10 wt%, (d) 15 wt%, (e) 20 wt%, and (f) 30 wt% sodium citrate embedded nanofibers. (scale bar size: 10  $\mu$ m).

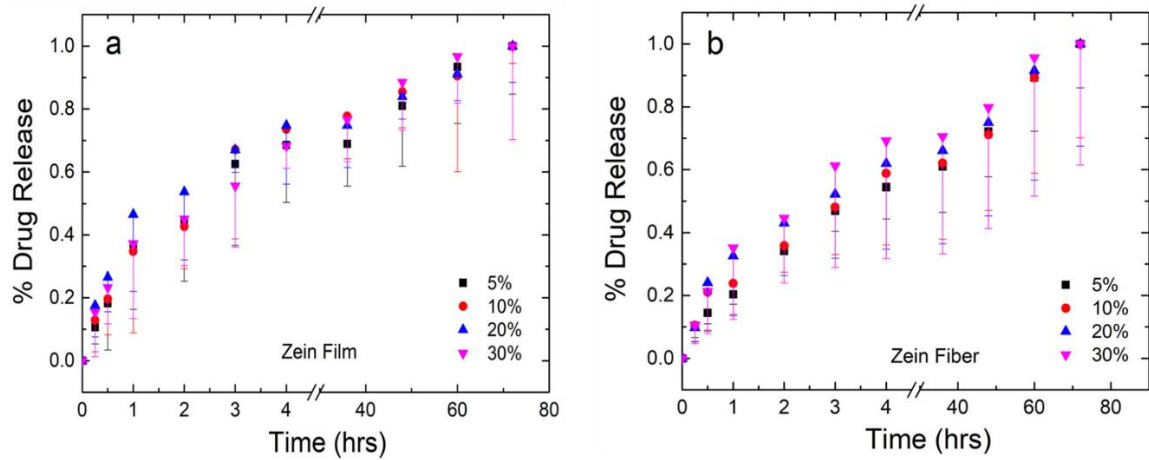
### **2.3.5 Drug Release Profile**

The release of sodium citrate from corn zein nanofibers and thin films was compared by plotting the cumulative mass released from both samples over a 72-h time period. The mass of citrate released from each set of samples was averaged and normalized to 100% released at 72-h. Error bars were added to the thin film plot in Figure

2.8a based on standard deviation and to the fiber plot in Figure 2.8b based on the average mass lost to degradation of pure zein fibers in water.

**Figure 2.8**

*Release Profiles of Sodium Citrate from Corn Zein Nanofibers and Thin Films*



*Note.* Normalized release profiles of sodium citrate from corn zein films (a) and fibers (b). Content of sodium citrate ranged 5 to 30 wt% drug/zein with samples taken between 0.25–72 h.

In both the film and the fiber samples, most of the embedded sodium citrate is released in the first 6 h of soaking. There is a biphasic release in all samples, but fiber samples plateau at a lower percentage (45-60%) than films do (60-75%). From 52-72 h, the remainder of the citrate is released from the samples. During the initial release, before

the plateau period, corn zein films release citrate slower than the nanofibers due. Beyond the plateau, the reverse becomes true; films release citrate faster than nanofibers from 52-72h h. This is likely caused by charge-charge or hydrogen bonding interactions between the citrate molecules themselves since the molecules contain an alcohol and several carbonyl groups. Once a majority of the citrate has been released (>75%), citrate molecules are less prevalent for self-interaction, which leads to faster release and dissolution. This trend is most obvious with the 30 wt% citrate films (Figure 2.8a, pink triangles).

Fiber samples generally have a slower, more controlled release of citrate as indicated by their lower plateau. This is expected and reported in several other drug release studies due to the large surface area-to-volume ratio that nanofibers provide<sup>8, 129, 159, 160</sup>. This controlled release is also caused by the molecular interactions seen in the FTIR analysis, where citrate molecules interact with the protein structure of zein in nanofibers, but not in films.

To provide a quantitative comparison of citrate release between fibers and films, a paired two-sample t-test was performed for each wt% of citrate using Excel. The results are summarized in Table 2.2. All test results were compared to a T-critical of 1.812 at a 0.05 alpha significance level. With T-statistics of 3.948, 3.363, and 4.128 for 5, 10, and 20 wt% citrate being higher than the T-critical of 1.812, the null hypothesis for these groups was rejected. 30 wt% citrate had a T-statistic of 1.464, so the null hypothesis was accepted. Within this study, the null hypothesis was that there was no significant

difference in the mean mass of citrate released by films and fibers. Therefore, only the 30 wt% nanofibers had a statistically comparable drug release to their film counterparts. This was further supported by the calculated p values. Once again, 5, 10 and 20 wt% samples were determined to be significantly different with p values of 0.003, 0.007, and 0.002, respectively. For the 30 wt% group, a p value of 0.174 was calculated, indicating again that there was no significantly different release of citrate between the fibers and the films. Comparing these results to the morphology analysis makes sense; at 30 wt% citrate, nanofibers lost their porous characteristics and became brittle, likening them to thin films rather than the porous nanofiber networks seen in the lower wt% samples. All four group analyzed showed Pearson correlation coefficients close to 1, indicating high linear correlation.

**Table 2.2**

*Statistical Comparison of Citrate Release from Zein Nanofibers and Thin Films*

<i>Citrate wt%</i>	<i>Pearson Correlation</i>	<i>T-Statistic</i>	<i>p (T≤t)</i>
5%	0.983	3.948	0.003
10%	0.977	3.363	0.007
20%	0.984	4.128	0.002
30%	0.993	1.464	0.174

*Note.* Summary of important statistics obtained from a paired two sample t-test between the average mass of citrate released from fiber and film samples at each citrate wt%. All samples were analyzed with an alpha level of 0.05 and a t-critical of 1.812.

### ***2.3.6 Cell Compatibility and Effect of Sodium Citrate Release***

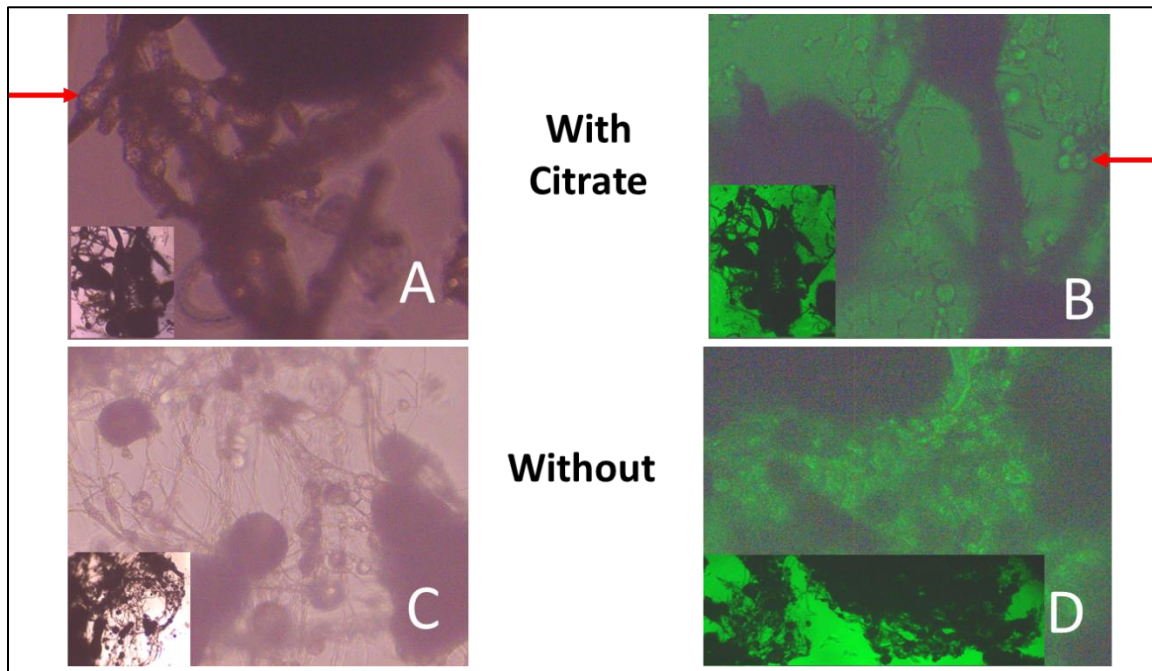
To demonstrate the potential of zein nanofibers for topical drug delivery, cell biocompatibility studies were performed using human embryonic kidney cells (HEK293). Cells were cultured on zein fibrous mats embedded with 0-30 wt% sodium citrate for 72 h. Cells were also cultured on a plastic petri dish as a control. After 72 h, light



microscopy was used to study the morphology of the cells on the materials (Figure 2.9). The morphology on the zein materials was comparable to that of the control.

**Figure 2.9**

*Light Microscopy of HEK293 Cells on Zein-Citrate Fibrous Mats*



*Note.* Cell morphology on zein fibrous mats is comparable to that of the control.

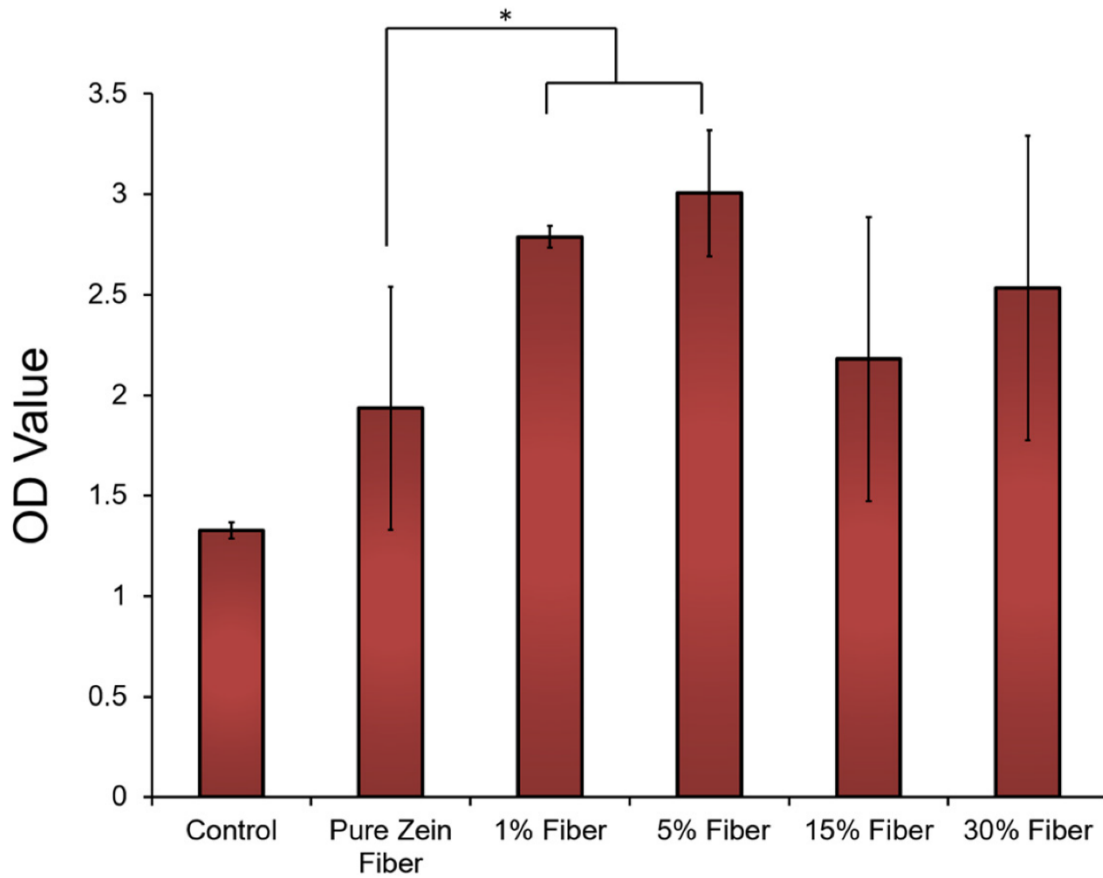
Following microscopy, the metabolic activity of the cells was evaluated using an MTT assay (Figure 2.10). When compared with the control, zein fibrous materials showed a significantly increased metabolism, indicating enhanced proliferation of cells



on the zein fibers. It was also seen that at lower concentrations of sodium citrate (<15%) there was an increase in metabolism compared to zein without sodium citrate, indicating that the addition of citrate could improve the health of cells in biomedical applications. At higher amounts of citrate, however (>15%), the metabolic activity of the cells becomes lower. This could indicate that the release of sodium citrate in the materials inhibits cell proliferation, although it could also be a result of the change in fiber morphology at these higher amounts of citrate as seen in the SEM analysis. The increase in fiber diameter and decrease in porosity at these higher amounts of citrate limits the transport of sodium citrate through the material and reduces drug-cell interactions. Significant differences in cell metabolism was confirmed by T-Test between sample groups with a significance value of 0.05.

**Figure 2.10**

*MTT Assay of 72-h HEK293 Cell Culture on Zein-Citrate Fibrous Mats*

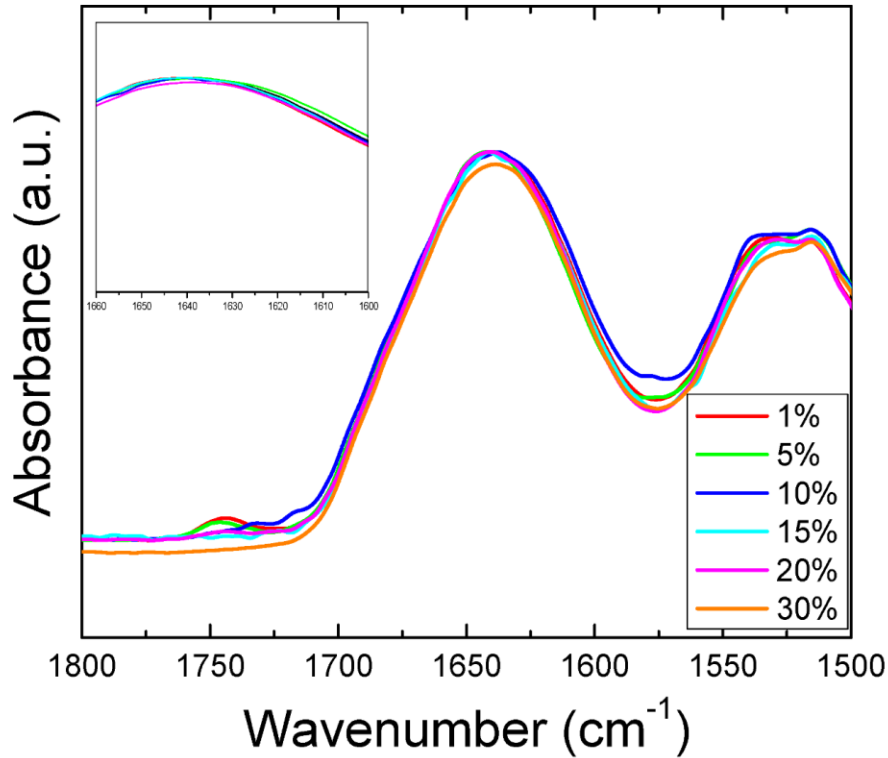


*Note.* HEK293 (Human embryonic kidney) cells cultured on zein fibrous mats for 72 h showed improved metabolic activity compared to a control petri dish. T-tests were performed between indicated groups (\*  $p < 0.05$ ).

To study the effects of the release of sodium citrate from the materials on the zein protein structure, embedded nanofibers were analyzed by FTIR again after soaking in PBS for 72 h (Figure 2.11). Upon release of sodium citrate, zein nanofibers revert back to their original random coil structure indicated by the absorbance peak at  $1640\text{ cm}^{-1}$ . In addition, the peak at  $1720\text{ cm}^{-1}$  caused by C=O stretching between the zein protein chains and sodium citrate molecules disappears, further confirming the interaction inferred in the initial FTIR analysis. This makes zein protein an ideal candidate for drug delivery applications, since therapeutic molecules cause stabilizing interactions, but do not permanently alter the protein structure on the molecular scale.

**Figure 2.11**

*FTIR Analysis on Zein Nanofibers after Citrate Release*



*Note.* Absorbance in the Amide I region in all zein fiber samples reverts to the 1640 cm<sup>-1</sup> seen in zein fibers without citrate. This indicates a reversible transition back to the original random coil structure of zein before citrate was embedded.

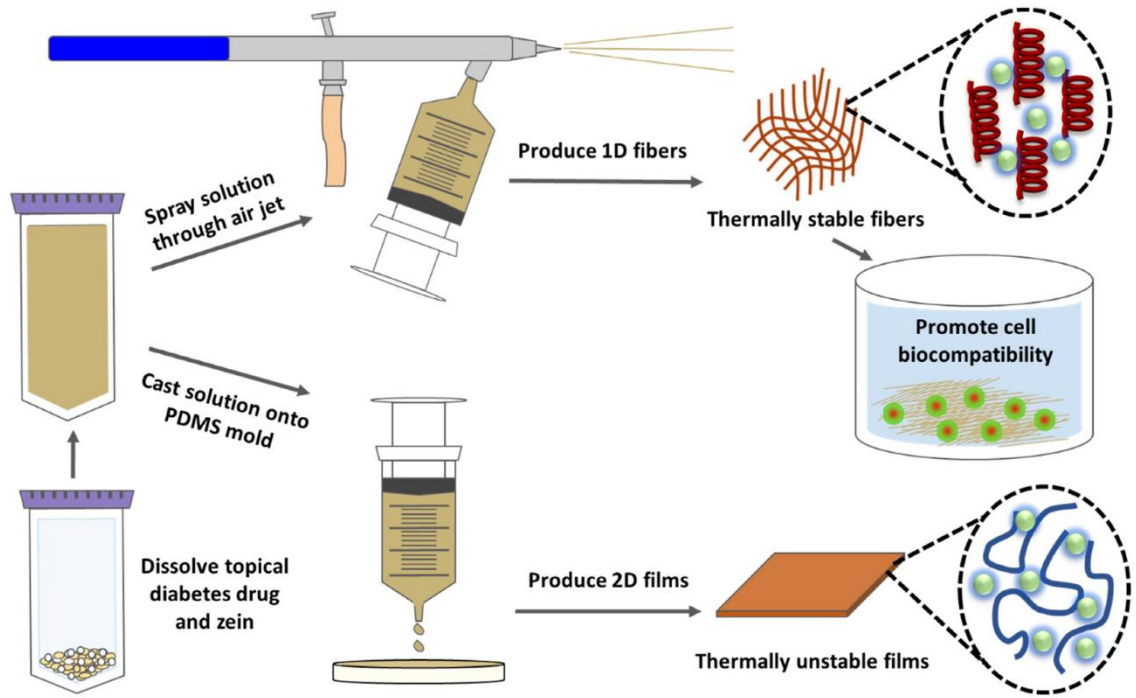
### **2.3.7 Mechanism**

The increased thermal stability of zein nanofibers compared to zein films is likely due to stabilizing interactions between sodium citrate and zein protein in the nanofibers.

As seen in the Amide I and II regions of the FTIR spectra, citrate-embedded fibers shift their protein structure from a random coil network towards an alpha helical conformation. Since alpha helices are stabilized by hydrogen bonding, it is plausible that the same interaction between citrate molecules and the zein protein structure that causes a shift in protein structure is also responsible for the higher degradation temperature of the fibers. This interaction was not seen in the films, which degrade at lower temperatures than the fibers. Thermal analysis was also able to confirm that in samples with more citrate, there is a reduction in degradation. This is seen as a more gradual change in mass in the TGA thermograms and sharper changes in reversing heat capacity in the DSC thermograms. Embedded zein films do not see these same properties because of the lack of interaction between sodium citrate and the zein protein structure. Despite hydrogen bonding between sodium citrate and the protein structure in zein fibers, the change in protein conformation is reversible upon release of citrate. This makes zein protein a useful candidate for drug delivery applications, since therapeutic molecules can interact with the protein structure to stabilize the composite without permanently altering the structure of the protein making up the majority of the composite. Figure 2.12 illustrates these interactions and results.

**Figure 2.12**

*Mechanism of Interaction*



*Note.* Sodium citrate is embedded into 1D zein fibers or 2D zein films. 1D zein fibers have higher thermal stability and promote cell biocompatibility.

## 2.4 Conclusions

Corn zein fibrous nanofibers proved to be an effective carrier for sodium citrate, which can be delivered topically as a patch to treat diabetic ulcers. Analysis of the zein protein structure through FTIR showed that sodium citrate can interact with zein to shift its protein structure from an unstable random coil to a stabilized alpha helical network.

The same interaction was not seen in corn zein films. This interaction resulted in a slower, more controlled release of sodium citrate from the nanofibers compared to the films, but did not permanently alter the protein structure. Upon release of citrate, zein nanofibers reverted back to their original random coil structure. At the same time, the alpha helical structure induced by sodium citrate improved the thermal stability of corn zein fibers, resulting in a higher degradation temperature than their film counterparts. This thermal stability was confirmed by DSC and TGA analysis. Despite this, there is a limit to sodium citrate content exists where nanofibers begin to lose their porosity and nanoscale diameter, which limits their usefulness as a drug delivery carrier and the ability of cells to proliferate in the fiber network. SEM morphology analysis as well as biocompatibility studies confirm this. Because of this, a lower concentration of sodium citrate (5~15%) may be more suitable for biomedical applications. Despite this limitation, zein nanofibers still show promise with the potential to be used for the delivery of other therapeutic molecules. The unique tunability of biomaterials provide many means of modifying the physicochemical properties of the material to cater to specific applications as needed to accompany different therapies and patients. We envision the combination of these corn zein mats with sensors to detect swelling which will alert patients or providers to administer a new dose of sodium citrate to treat diabetic ulcers.

## Chapter 3

### Study of Silk-Based Thin Films and Air-Spun Nanofibers for Topical Drug Delivery Using Various Model Drugs

#### 3.1 Introduction

An emerging field of research aiming to solve many of the current problems with drug delivery is protein-based drug delivery vehicles<sup>136</sup>. Very frequently, protein biomaterials in the form of nanofibers<sup>8, 9, 23, 111, 112, 131, 136, 161</sup> or thin films<sup>8, 9, 23, 111, 130, 136</sup> are fabricated to delivery therapeutics. These types of delivery vehicles provide many benefits over systemic delivery, mostly by reducing off-target effects and lowering dosage requirements to improve patient compliance<sup>136, 162</sup>. This study places particular interest on nanofibers due to their high surface-area-to-volume ratio and high porosity, which improve drug loading efficiency and enhance mass transfer properties<sup>8, 36, 97, 161, 163</sup>. Because of their protein origin, protein-based nanofibers provide additional biocompatibility, biodegradability, and bioactivity due to differing protein structures and amino acid sequences that allow biochemical and biophysical interactions with therapeutics<sup>55, 164</sup>. Today, protein-based nanofibers are limited in clinical use due to a lack of quantitative data and the need for a reliable large-scale production method<sup>165</sup>.

One solution for the plausible scale-up production of nanofibers is through air-spraying or solution blowing. To date, the most common nanofiber fabrication methods are electrospinning and techniques directly related to it<sup>94, 166-169</sup>. Electrospinning works by connecting the outlet of a spinneret to a high voltage power source. When surface



tension in the polymer solution is overcome by electrostatic forces, the polymer is drawn into fibers to be collected on a grounded surface or a collection bath<sup>170</sup>. The need for a high voltage power source makes this method costly and dangerous, and the throughput is slow. This study utilized an alternative fiber fabrication technique known as air-spraying or solution spraying. Instead of high voltage, this method uses compressed air as the main driving force of fiber formation<sup>8, 36, 108, 150</sup>. A concentric nozzle is used where one inlet is fed polymer solution and the other is fed high pressure air from a compressor; the high-pressure air shears the polymer solution into strands of fibers, which quickly form solid fibers once the solution leaves the nozzle and the solvent evaporates off. The fibers can be collected on a range of substrates similar to electrospinning, but the process has a higher throughput<sup>108</sup> which makes it a potential method for large-scale nanofiber production.

Protein-based nanofibers can be made from a wide variety of proteins<sup>20, 55, 95, 105, 164</sup>, but this study chose to use *Bombyx mori* silk specifically due to its mechanical and thermal properties, chemical stability, and good biocompatibility<sup>87</sup>. In nature, silk cocoons consist of two major components: silk fibroin protein and sticky sericin proteins. By boiling the cocoons in weak saltwater, one can separate the silk fibroin to produce silk biomaterials in several different forms<sup>10, 31, 90, 103, 154, 168, 171, 172</sup>. Depending on the source, silk can contain slightly differing protein structures due to differing amino acid structures. *Bombyx mori* silk owes its strong mechanical properties to intermolecular beta sheets that form due to the amino acid sequence<sup>173</sup>. These beta sheets also enhance the bioactivity of silk, allowing for tunable properties by tailoring the beta sheet content in

the silk to change its mechanical properties or tailor the release of drugs from the biomaterial structure<sup>32, 174</sup>.

Several studies (cited above) have focused on the use of silk films for controlled drug delivery, but little research has been done using silk nanofibers for the same purpose. The strong mass transfer benefits of nanofibers, coupled with the ability to tailor crystallinity (beta sheets) in silk, provide a promising platform for the controlled release of therapeutic molecules. Within this study, the porous 1D geometry of silk nanofibers was compared to the flat 2D geometry of silk films with respect to the release profile of several model drugs. These models varied in weight, charge, water solubility, and hydrophobicity, and were chosen to reflect the type of drugs used in the market today. FTIR, SEM, TGA, and DSC were all used to study the effects the model drugs had on the protein structure of silk biomaterials and their subsequent release from the biomaterials. The release profiles of the model drugs were also studied in order to compare the effects of biomaterial geometry on release speeds.

## **3.2 Materials and Methods**

### ***3.2.1 Materials Preparation***

Silk cocoons from the *Bombyx mori* silkworm were purchased from Treenway Silks. Prior to use, the silk fibroin protein was separated from the sticky sericin proteins by boiling cocoons in a 0.02 M NaHCO<sub>3</sub> (Sigma-Aldrich) solution for 15 minutes. Silk fibroin fibers were then washed in deionized water for 15 minutes, four times, and dried in an oven at 60 °C overnight. To dissolve silk fibroin, a solution of 4% wt./vol CaCl<sub>2</sub>

was prepared using CaCl<sub>2</sub> from AMRESCO and 98% grade ACS purity formic acid from EMD Millipore. Crystal violet, indigo carmine, alcian blue 8GX, rhodamine B, and rifampin (rifampicin) were used as-is from VWR International.

### ***3.2.2 Silk Nanofibers***

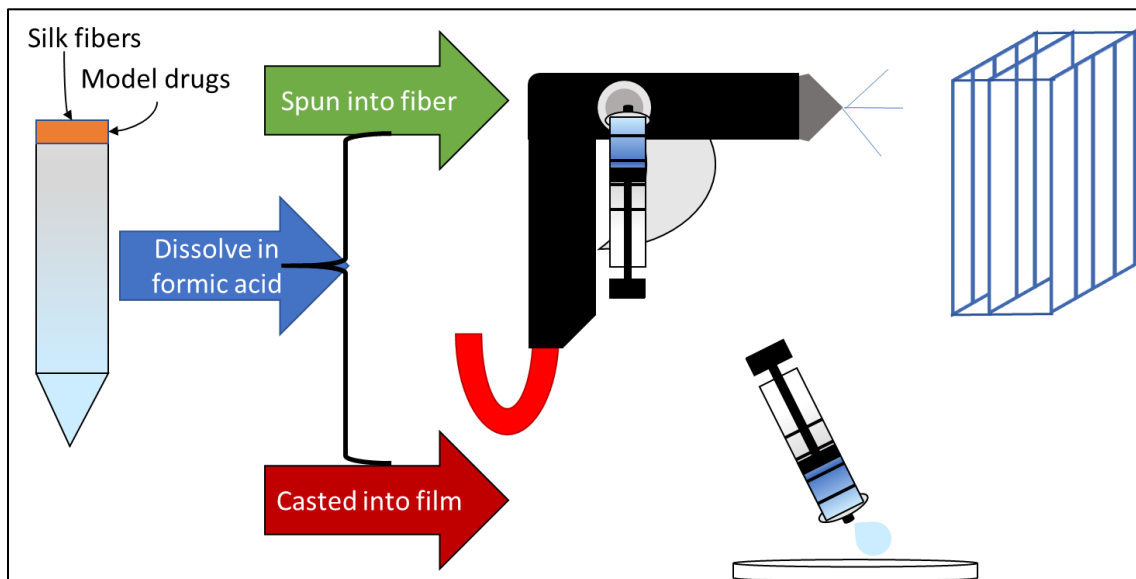
Oven-dried (60 °C) silk fibroin fibers were used to fabricate silk nanofibers. 0.75 g of silk fibers was dissolved into 5 mL of 4% CaCl<sub>2</sub> formic acid solution based on prior studies<sup>154</sup>. At this concentration, silk nanofibers maintain the high mechanical strength and thermal stability of silk, but the concentration is low enough to prevent clogging of the spray gun. For model drug-embedded silk fibers, 0.05 g (1% wt./vol) was dissolved in CaCl<sub>2</sub> formic acid before adding silk. To facilitate dissolution, a benchtop vortexer was used, following by centrifugation at 2000 RCF for 10 minutes. Once the solution was homogeneous and free of aggregates, the solution was transferred to a Leur-Lok syringe to be sprayed through a high-pressure low volume (HPLV) gravity-feed spray gun. The spray gun was fed ultra-dry air at 80 psi to shear the solution into fibers which were collected on a grated substrate roughly 20 cm away from the nozzle. Fine-tuning of the air pressure, spray angle, and fluid intake was controlled via knobs on the spray gun to optimize fiber formation. In most situations, the smallest spray angle, lower fluid intake, and lower pressure was optimal. The relative humidity in the environment varied from 20-22% during fabrication. All fibers were collected from the substrate immediately after spraying and transferred to storage in a vacuum oven at 60 °C overnight (12+ hours) to

remove any excess  $\text{CaCl}_2$  formic acid solution that did not evaporate during air spraying.

Figure 3.1 (top path) below illustrates the process.

**Figure 3.1**

*Silk Biomaterial Synthesis*

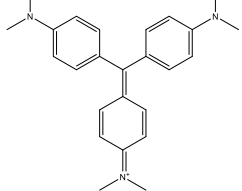
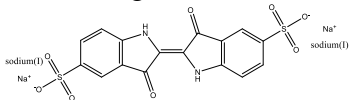
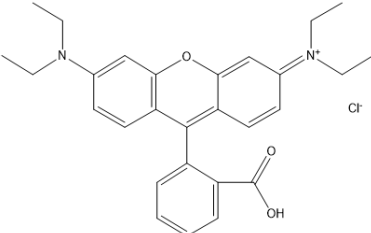
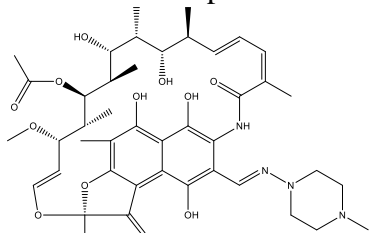
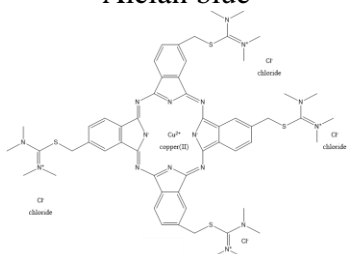


*Note.* Silk-model drug solutions were spun into nanofibers via spray gun or casted onto PDMS molds for film fabrication.

The choice of model drugs in this study were chosen based on the library of pharmaceutical compounds in the pharmacopeia. They represent a varying set of physicochemical properties including in their molecular weight, solubility, charge, and

hydrophobicity (Table 3.1). All model drugs had distinct, measurable absorbance within the UV-visible light spectrum, proving a reliable quantification assay for measuring their release from the biomaterials. A very small amount of the drug was detectable, which helped to prevent model drug crystals from clogging the spray gun.

**Table 3.1***Physicochemical Properties of Model Drugs<sup>8</sup>*

Model Drug	Molecular Weight (g/mol)	Solubility in Water at 25 °C (g/L)	Log P
<b>Crystal violet</b> 	407.98	50	1.4
<b>Indigo carmine</b> 	466.36	10	1.01
<b>Rhodamine B</b> 	497.02	9	1.95
<b>Rifampin</b> 	822.94	2.5	2.77
<b>Alcian blue</b> 	1298.9	1	-9.7

### ***3.2.3 Silk Films***

To compare the effects of biomaterial structure and morphology on release kinetics, 2D silk films were also fabricated and embedded with model drugs. Silk solutions were prepared in the same way as they were prepared for fibers, but only 3 mL of the solution was cast onto circular PDMS molds for film fabrication (Figure 3.1, bottom path). Solutions plasticized at room temperature for 48 h to allow films to form; drying in a vacuum oven at 60 °C for 12 h after film formation assisted in evaporating excess solvent before any characterization tests were performed.

### ***3.2.4 Morphology Characterization***

Characterization of the silk biomaterial morphology was performed using Scanning Electron Microscopy (SEM) imagery from a Zeiss Leo 1530 VP SEM. Samples were sputter coated in gold to improve their conductivity, followed by image at 100, 500, 1000, 2000, and 5000x at an EHT of 5.00 kV. Not all images are displayed in this thesis. ImageJ image processing software was used to measure the average diameter of the fiber samples to study the effects of drug loading on fiber morphology as well as the general size of fibers produced by air spraying.

### ***3.2.5 Fourier Transform Infrared Spectrometry (FTIR)***

Additional morphology analysis was performed by using Fourier Transform Infrared Spectroscopy (FTIR) to study the protein structure in the biomaterials. A Bruker Tensor 27 Fourier Transform Infrared Spectrometer with deuterated triglycine sulfate

detector and multiple reflection horizontal MIRacle Attenuated Total Reflection (ATR) attachment, fitted with a Ge crystal, was used to obtain the spectra. Readings were taken from 4000 to 400  $\text{cm}^{-1}$  with a resolution of 4  $\text{cm}^{-1}$ . All samples were read with 64 samples scans and 64 background scans, and readings were taken at least twice on each side to ensure homogeneity throughout the sample. Between different samples, the ATR crystal was cleaned with methanol.

### ***3.2.6 Differential Scanning Calorimetry (DSC)***

Thermal analysis was first performed using Temperature-modulated Differential Scanning Calorimetry (TM-DSC) with a Q100 DSC from TA Instruments. The instrument was equipped with a refrigerated cooling system and purged with nitrogen gas at a rate of 50 mL/min. Before any samples were analyzed, the instrument was calibrated for heat flow and temperature using indium and for heat capacity with aluminum and sapphire reference standards. Small samples (5-7 mg) were captured in aluminum pans and heated at a rate of 2  $^{\circ}\text{C}/\text{min}$  from -40 to 400  $^{\circ}\text{C}$ . TM-DSC parameters included an amplitude of 0.318  $^{\circ}\text{C}$  and a modulation period of 60 s.

### ***3.2.7 Thermal Gravimetric Analysis (TGA)***

Further insight to the thermal integrity of silk fibers and films was studied by Thermal Gravimetric Analysis (TGA) using an SDT-Q600 TGA from TA Instruments with 100 mL/min nitrogen purge gas flow. Small (4-6 mg) samples were heated from 25-800  $^{\circ}\text{C}$  at a rate of 10  $^{\circ}\text{C}/\text{min}$  while recording their mass.



### ***3.2.8 Drug Release Study***

Small (6 mg) triplicate samples of silk fibers and films were submerged in 40 mL of deionized water to stimulate the release of model drugs from the samples. Control samples of pure silk fibers and films without model drugs were also immersed in water. Over the course of four days, 200  $\mu$ L of the solution samples were soaking in was removed and placed into a 96 well plate for analysis later. These aliquots were taken at predetermined time points (15 min, 30 min, 45 min, 1 h, 2 h, 3 h, 4 h, 5 h, 6 h, 12 h, 24 h, 36 h, 48 h, 60 h, 72 h, 84 h, 96 h) to study the release kinetics of the model drugs from the biomaterials. Between sampling, well plates were covered to prevent contamination or loss of aliquots. After all aliquots were collected, the UV-visible absorbance of each was quantified using a SpectraMax i3x Plate Reader from Molecular Devices LLC. Readings were taken horizontally across each well with 10 readings spaced 0.57 mm apart. The specific wavelength for each set of model drugs varied depending on the lambda max of the drug, which was determined through absorbance testing across the UV-visible spectrum first. Once outliers were removed from the data, the remaining absorbance readings were normalized from 0 to 1 to compare the release kinetics across different model drugs and across fibers and films. A two sample Student's T-Test was performed across fiber and film samples for each model drug in order to test for statistically significant release speeds. All samples were removed from deionized water and dried for 12 h at 60 °C after release testing to re-analyze them by FTIR.

### 3.3 Results and Discussion

#### 3.3.1 Structural Characterization

Structural properties of air-spun silk fibers both with and without embedded model drugs was initially studied using FTIR. Figure 3.2a depicts the full spectra for all samples. These spectra proved that the formic acid used for fabrication evaporated off during fiber spraying or drying afterwards evident by the lack of a C=O ketone peak in the 1745-1715  $\text{cm}^{-1}$  region. All peaks show a relatively similar amplitude among all samples.

Special attention was given to the Amide I and II regions of the FTIR spectra to understand how material fabrication and addition of model drugs affected the protein structure of the silk fibers. This region, highlighted in Figure 3.2b, is frequently used to analyze the secondary structures of proteins.<sup>86</sup> Stretching vibrations between C=O molecules in the protein backbone are the main contributor to the amide I region, which ranges from 1600-1700  $\text{cm}^{-1}$ . There are also some minor contributions from C-C $\equiv$ N deformation, C $\equiv$ N stretching out-of-phase, and N-H in-plane stretching. The amide II region, meanwhile, is caused by IR absorption of an out-of-phase combination of vibrations of C-N stretching and N-H bending in-plane, which shows up between 1600-1500  $\text{cm}^{-1}$ .<sup>154</sup> FTIR analysis on the silk fibers revealed an absorbance peak centered at 1639  $\text{cm}^{-1}$ , which is indicative of intramolecular  $\beta$ -sheets suspended in a random coil network<sup>153, 175-179</sup>. The addition of model drugs was able to produce some shifting of this peak (Figure 3.2b, embedded). Specifically, alcian blue and rhodamine B shift the

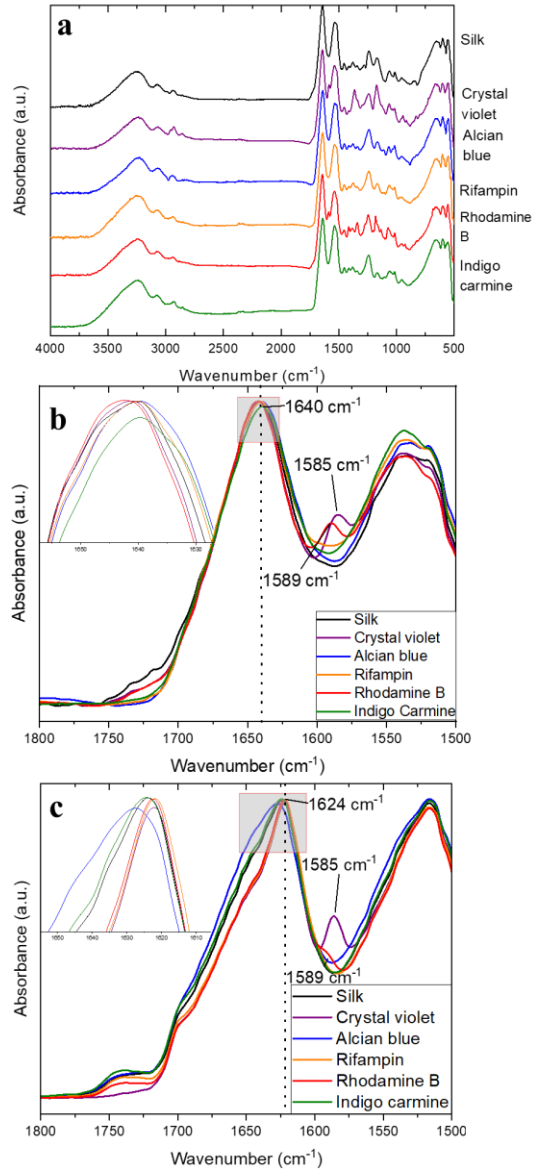
absorbance peak to  $1641\text{ cm}^{-1}$  while rifampin shifts the peak to  $1640\text{ cm}^{-1}$ . Additional shoulders also appear at  $1585\text{ cm}^{-1}$  and  $1589\text{ cm}^{-1}$  for crystal violet and rhodamine B embedded fibers, respectively. Both of these absorbances are caused by the model drugs themselves based on FTIR spectra of aqueous solutions of the model drugs.<sup>8</sup> There is also an increased absorbance at  $1720\text{ cm}^{-1}$  in some embedded samples. Absorptions at this wavenumber are indicative of C=O stretching of the protein backbone<sup>180, 181</sup> further supporting the idea of molecular interaction between model drugs and the silk protein structure. Alcian blue and rhodamine B are both very hydrophobic molecules with high log P values of 2.77 and 1.95, respectively, which suggest that hydrophobicity of the embedded molecules could play a role in driving the self-assembly of silk into ordered secondary structures. This is similar to the complex interactions that amine additives have to suppress or assist in protein interactions<sup>182</sup>. By understanding the biophysical and chemical nature of therapeutic molecules, it may be possible to produce fine-tuned protein-based biomaterials by tailoring the molecular interactions between the protein structure and the biomaterial's therapeutic load.

Silk fibers were soaked in water for 4 days to release the model drugs from them and then re-analyzed by FTIR. This analysis must be prefaced with the observation that water soaking causes a release of  $\text{CaCl}_2$  ions that were introduced by the solvent to act as plasticizers and prevent intermolecular  $\beta$ -sheet formation. Upon removal of these ions, silk is able to re-form its native intermolecular beta sheet structure<sup>88, 154, 170</sup>. Therefore, this transition in protein structure is not a primary result of the model drugs releasing. FTIR spectra (Figure 3.2c) revealed this transition to be the case in this study. After a

four day soak, all silk nanofibers, with or without embedded model drugs, shifted from amorphous silk I structure to crystalline silk II structure based on the new absorbance peaks between 1622-1628  $\text{cm}^{-1}$  <sup>153, 154</sup>. Other changes in the FTIR spectra include decreases in the characteristic peaks of crystal violet at 1585  $\text{cm}^{-1}$  and rhodamine B at 1589  $\text{cm}^{-1}$  due to the release of most of the molecules from the fibers. The variance in absorbance peak for the silk fibers is more indication of molecular interactions between the model drugs and silk protein structure. Pure silk sees this absorbance peak centered at 1624  $\text{cm}^{-1}$ , but the physiochemical properties, especially the hydrophobicity, of the model drugs impact the self-folding of silk protein into intermolecular  $\beta$ -sheets. Alcian blue, with the highest weight and the most hydrophobicity, restricts the formation of intermolecular  $\beta$ -sheets based on a smaller shift in its absorbance peak at 1628  $\text{cm}^{-1}$ . On the other hand, rhodamine B and indigo carmine, with lower hydrophobicity, and rifampin with a hydrophilic character, help facilitate the formation of intermolecular  $\beta$ -sheets indicated by an absorbance peak at 1622  $\text{cm}^{-1}$ . These interactions are further evidence that the compatibility of molecules and proteins are a crucial aspect of designing tunable biomaterials with tailored mechanical properties or release mechanisms. When coupled with the high porosity, surface-area-to-volume ratio, and malleability of nanofibers, there is clear potential for protein-based nanofibers in drug delivery.

**Figure 3.2**

*FTIR Spectra of Silk Fibers*



*Note.* FTIR spectra for silk and silk-drug fibers. (a) Full spectra of fibers before drug release. (b) Amide I and II regions shown to emphasized protein structure. (c) Amide I and II regions after release of model drugs.

A parallel analysis was performed on silk films with and without embedded model drugs. The full spectra (Figure 3.3a) again shows the absence of a formic acid peak, indicating that excess formic acid  $\text{CaCl}_2$  solvent was evaporated during film formation or drying.

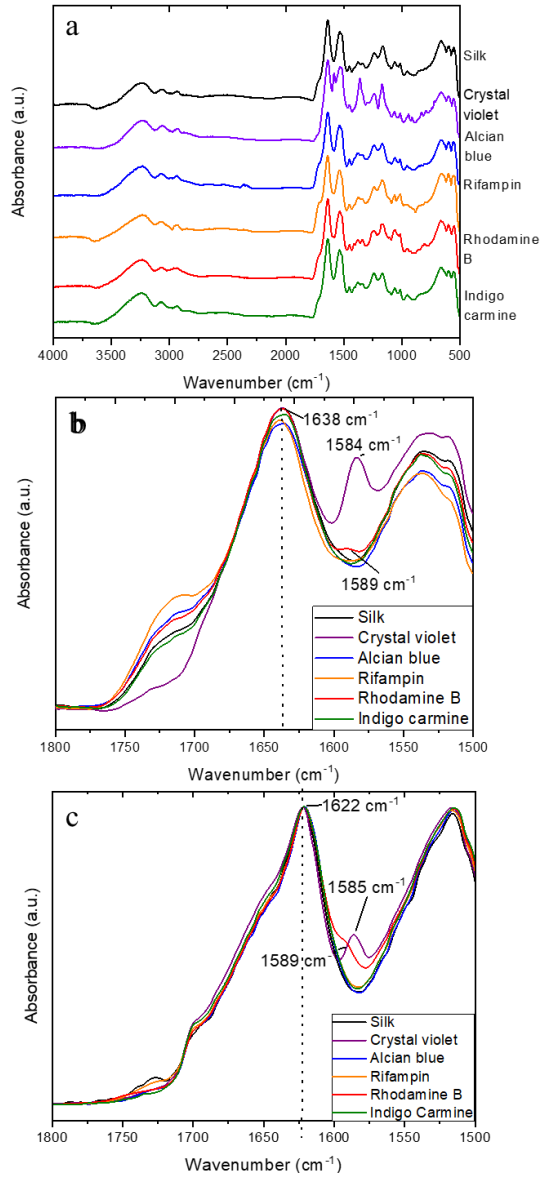
The amide I and II regions were again closely examined for changes in secondary protein structure (Figure 3.3b). Prior to water soaking, all film samples showed an absorbance peak centered at  $1640\text{ cm}^{-1}$  which is again indicative of amorphous silk I structure containing a majority of random coils and some intramolecular  $\beta$ -sheets. Crystal violet and rhodamine B showed their characteristic peaks again, indicating adequate embedment of the model drugs within the films. Unlike the fiber samples, there is no variance in absorbance. In the larger, nonporous, 2D geometry of silk films, the model drugs were unable to influence the self-assembly of silk enough to change their IR absorbance spectra. Because silk fibers differed with porous, 1D geometry, there was greater opportunity for the model drugs to interact with the silk protein structure, allowing for shifts in the IR spectra. The lack of interaction between model drugs and the protein structure in silk films leads to lower thermal stability and control of the model drug release, which is revealed in more detail during thermal analysis and drug release testing later in this study.

After soaking in water and release of the model drugs, the film samples all shift to a crystalline silk II structure with high content of intermolecular  $\beta$ -sheets based on their IR absorbance peak at  $1622\text{ cm}^{-1}$  in Figure 3.3c. Like during their initial analysis, there is

no variation in secondary protein structure because the model drugs are unable to interact with the silk film protein structure well due to geometric constraints. This means the hydrophobicity and physicochemistry of the model drugs does not restrict the self-folding of silk into intermolecular  $\beta$ -sheets once  $\text{CaCl}_2$  ions are washed out by the water but limits the tunability of the films as a drug release vehicle.

**Figure 3.3**

*FTIR Spectra of Silk Films*



*Note.* (a) Full spectra of silk-model drug thin films before drug release. (b) Amide I and II regions shown to emphasized protein structure. (c) Amide II and II regions after release of model drugs.



### 3.3.2 Thermal Analysis

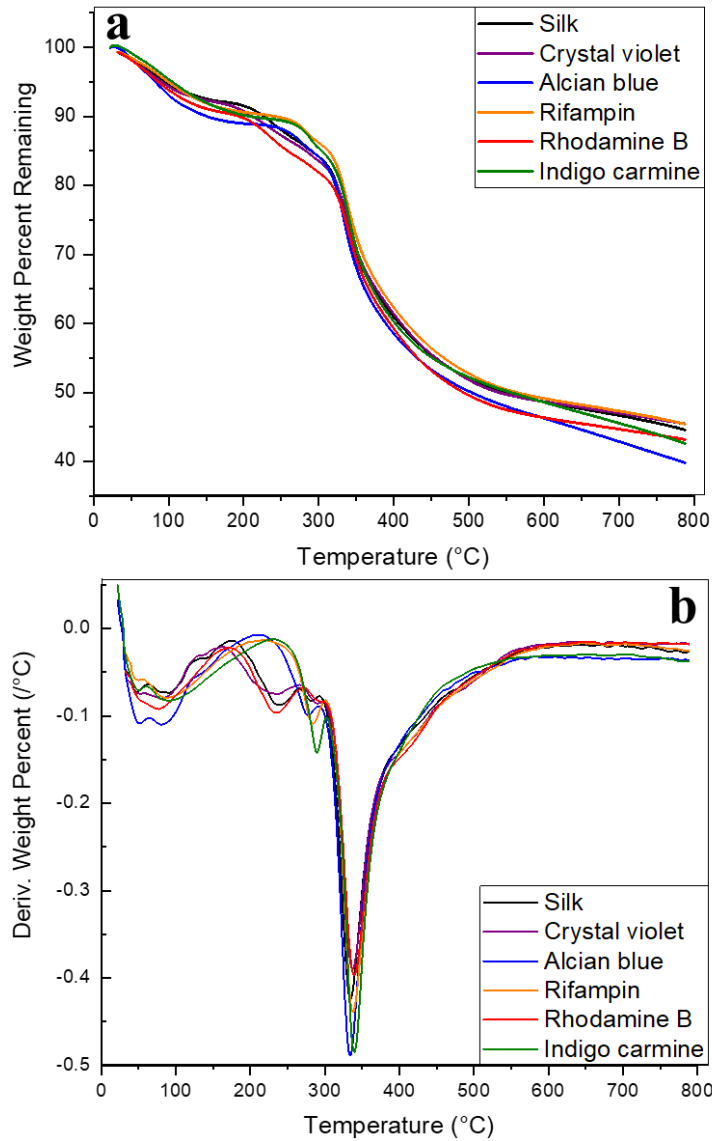
To first understand the overall thermal integrity of the silk fibers and films with and without embedded model drugs, TGA was used. The respective thermograms for fiber samples are shown in Figure 3.4. Within the weight percentage thermogram (Figure 3.4a) there is a small mass loss under 100 °C as excess water and solvent embedded in the fiber network is evaporated. There is then a gradual mass loss between 200-325 °C until major degradation begins. Once the samples reach 500 °C, major degradation slows or stops. By the end of the test at 800 °C, silk fibers maintain between 40-50% of their initial weight.

The effects of model drugs on the thermal stability was then studied. In embedded samples where the model drug pushed the protein structure towards higher  $\beta$ -sheet content (rifampin and indigo carmine), the onset of major degradation was delayed from 230 °C to 280 °C. Rhodamine B, which also influenced the FTIR absorbance in the amide I region, did not delay major degradation, but was able to stabilize the fiber materials in another way by slowing the rate of degradation. This is better seen in the derivative graph (Figure 3.4b) by the wide, shallow peak in the major degradation region. (350 °C). Alcian blue-embedded fibers also saw a later onset of degradation and slower degradation rate when compared to silk alone; degradation onset in alcian blue-embedded fibers did not begin until 280 °C whereas silk alone began degrading at 230 °C. Crystal violet, which did not change the IR absorbance much, does not push degradation onset

higher, but does slow major degradation in a manner similar to alcian blue-embedded fibers.

**Figure 3.4**

*TGA Thermograms of Silk-Model Drug Fibers*



*Note.* (a) Remaining weight percent of silk and silk-model drug fibers as they were heated to 800 °C. (b) Derivative of remaining weight percentage curves.

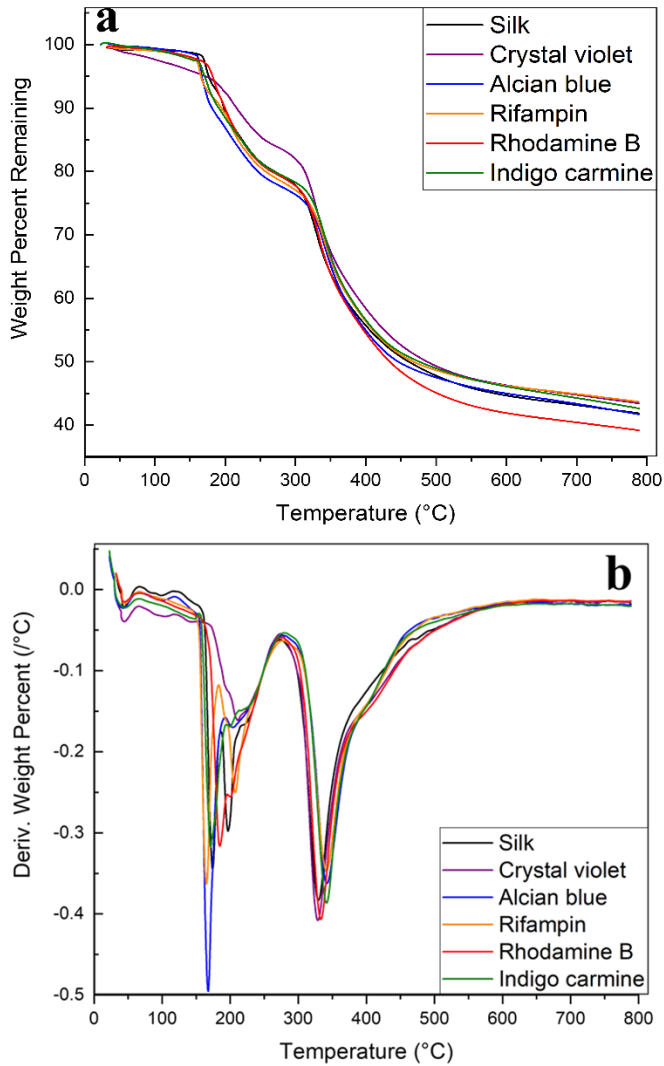
Silk films were also analyzed in the same way as the fibers. All film samples generally showed less thermal stability than their fiber counterparts (Figure 3.5). There is less degradation under 100 °C, although this is simply because any water or excess solvent is captured inside the 2D geometry of the films and cannot evaporate off. The samples themselves degrade earlier than the fibers do with sample degradation beginning around 180 °C. The samples also degrade much faster, whether with or without model drugs, indicative by the sharp derivative peaks in Figure 3.5b. Crystal violet-embedded films were best able to resist this degradation by showing a slower, constant degradation up to 200 °C. There are several sharp changes in mass at low temperatures (150-200 °C) in the thermograms of the model drug-embedded films, indicating that the 2D film geometry was unable to protect the model drugs from high temperatures like the fibers did. This cross-checks against the FTIR analysis, where model drugs were unable to interact with the silk protein structure inside the 2D film geometry. Model drugs in the 1D fibers, however, were able to interact with the silk protein during its self-assembly, which resulted in thermal protection. This is especially obvious in rifampin-embedded films. Rifampin is especially susceptible to thermal degradation with degradation as early as 183 °C and a cold storage requirement<sup>183</sup>. This can be seen clearly as a sharp peak in Figure 3.5b, but rifampin-embedded fibers containing the same amount of the model drug do not contain this same peak. Because rifampin was unable to interact with the silk film protein structure, it was not protected from thermal degradation. Instead of embedding within a fibrous network and interacting with the self-folding of silk, rifampin instead sits in layers in the nonporous 2D films and is easily degraded as temperatures approach its

degradation temperature. Similar behaviors of fibrous networks protecting therapeutic loads has been reported in other studies <sup>8, 36, 184</sup>.

Silk films also saw major degradation earlier than silk fibers did. Whereas fiber samples did not begin major degradation until 325 °C, films began degrading at 300 °C (Figure 3.5). The presence of model drugs influences the degradation rate of the samples in the major degradation region (325+ °C), although there are no trends or significantly different degradations like the fiber samples had. Regardless, rifampin, alcian blue, and indigo carmine show the most stabilization based on their smaller derivative peaks.

**Figure 3.5**

*TGA Thermograms of Silk-Model Drug Films*



*Note.* (a) Remaining weight percent of silk and silk-model drug thin films as they were heated to 800 °C. (b) Derivative of remaining weight percentage curves.

More precise thermal analysis was then performed using DSC. Beginning with fiber samples again, all samples see an initial small endothermic peak centered around 50 °C as excess solvent embedded within the fiber network evaporates (Figure 3.6a). This can be cross-referenced with the TGA thermograms, where silk fibers lost 5-10% of their initial mass as samples heated to 100 °C due to the evaporation of bound solvent. Although all of these peaks are roughly the same magnitude, they are slightly higher in samples embedded with rifampin, rhodamine B, and indigo violet- again the same model drugs that interacted with the protein structure of silk fibers. It is feasible that the interactions between the model drugs and the protein structure allowed more solvent into the fibrous network to bind to the protein. Between 250-350 °C, more endothermic peaks appear in all samples as degradation of the materials begins. Again, these temperatures correlate well to the degradation temperatures observed in the TGA thermograms. Rifampin-embedded silk fibers contain an additional peak near 155 °C which is likely connected to the degradation of the drug itself.

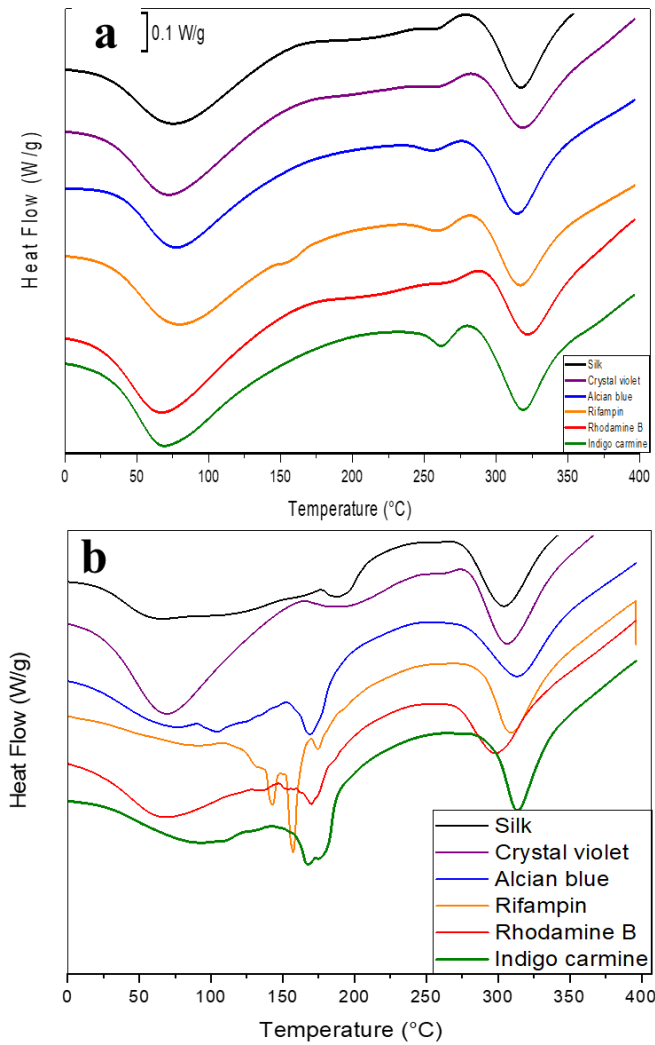
In comparison to the fibers, silk films have much noisier thermograms indicating lower thermal stability. This is further evidence that the model drug-silk protein interactions provide thermal stability, since these interactions were absent in the film FTIR spectra. Cross-referencing the TGA thermograms can help make sense of the noisy DSC thermograms. All of the model drugs except for crystal violet saw heavy degradation at 150 °C in TGA testing; as much as 0.5% mass/°C was lost from the film samples at this temperature. When translated to the DSC thermogram, this heavy degradation creates noise. Because of the nonporous 2D geometry of the films, the silk

protein structure was unable to protect most of the embedded drugs from thermal degradation in the same way the porous 1D fibers could. Crystal violet was the only drug protected from thermal degradation by the films. In addition to being the smallest model drug, crystal violet also contains a dimethylated aromatic tertiary amine which could interact with the carboxylic acids in the amino acids of the silk side chain. All of the larger model drugs with aromatic tertiary amines are diethylated, meaning crystal violet is also less sterically hindered than the other model drugs. Because of its smaller size and lower hindrance, it is not unreasonable that crystal violet can still have some biophysical and biochemical interactions with the silk protein structure in the films.



**Figure 3.6**

*DSC Total Heat Flow Thermograms of Silk-Model Drug Fibers and Films*



*Note.* Total heat flow graphs of silk and silk-model drug (a) fibers and (b) thin films.

Exothermic is upward.

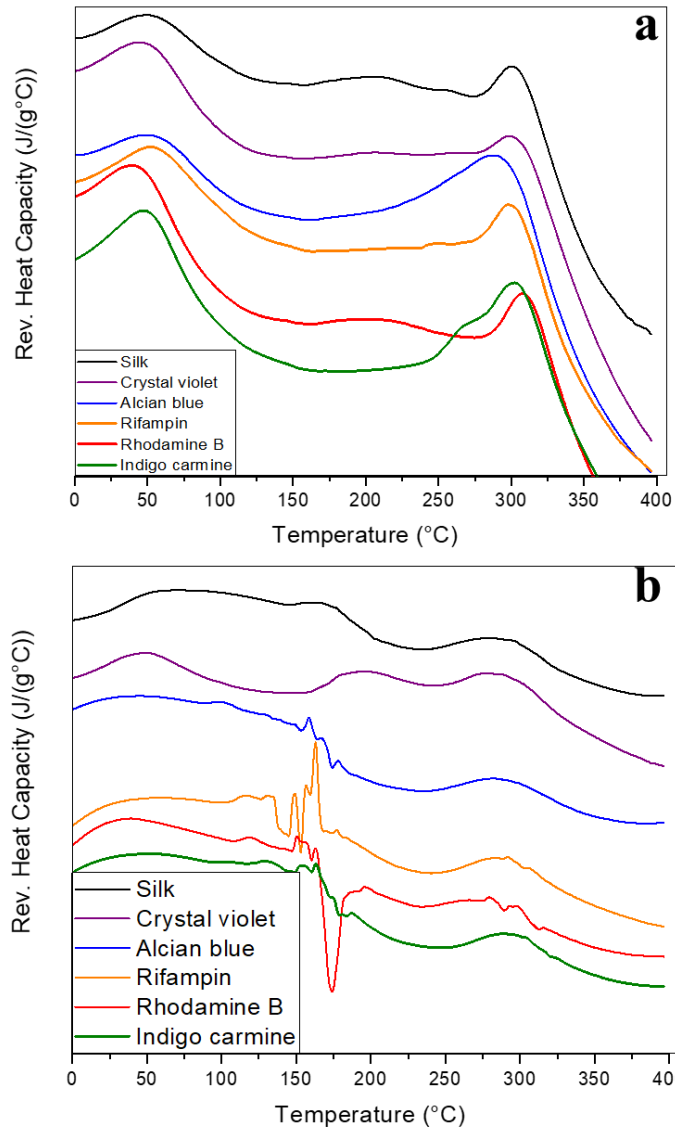
Further information about the thermal properties of the silk fibers was obtained by the reversing heat capacity thermograms produced by DSC (Figure 3.7a). Although some model drugs obscure glass transition temperatures ( $T_g$ ), they can still be identified in pure silk fibers and most model drug-embedded fibers. The most easily distinguishable  $T_g$  is found in pure silk fibers between 200-225 °C. Rhodamine B, crystal violet, and alcian blue-embedded fibers are less distinguishable; rifampin and indigo carmine-embedded fibers have indiscernible  $T_g$ s. Since rifampin degrades at 183 °C, it is possible that its melting and evaporation obscures reversing heat capacity changes caused by a glass transition. Since rifampin and indigo carmine-embedded fibers retained more of their mass before major degradation compared to silk fibers alone, it is possible that these influences on the thermal integrity of the silk fibers also influenced the visibility of a  $T_g$ . Similarly, rhodamine B-embedded fibers showed a slow, steady decomposition in the TGA thermogram, showing that it too may also influence heat capacity and the visibility of a  $T_g$ .

Although the reversing heat capacity thermograms of silk-model drug films are noisy like their heat flow graphs, some useful numbers can still be extracted from them (Figure 3.7b). All of the samples show an early glass transition around 50 °C as solvent internalized within the films plasticized. There is a similar trend to the fibers where model drugs cause some obscuring of this  $T_g$ ; in alcian blue, rifampin, and indigo carmine-embedded films, this obscurement makes the first  $T_g$  indiscernible. The film thermograms then move into the region where most of the drugs degrade, causing much noise and obscuring any useful changes in heat capacity. There is the possibility of a  $T_g$

in pure silk films and crystal violet-embedded films at 175 °C where silk films typically undergo a glass transition <sup>154</sup>, but all other samples are too noisy to detect a second T<sub>g</sub>, if one occurs. Once again, this thermal instability and the degradation of the drugs is due to poor interaction between the model drugs and the silk protein structure because of geometric constraints in the film geometry. Within the porous geometry of the fibrous materials, however, silk is better able to protect the model drugs from thermal degradation. Beyond this noisy region of the thermograms, all films begin major degradation around 300 °C which results in a decrease in heat capacity.

**Figure 3.7**

*DSC Reversing Heat Capacity Thermograms of Silk-Model Drug Fibers and Films*



*Note.* Reversing heat capacity of silk and silk-model drug (a) fibers and (b) thin films.

Exothermic is upward.

**Table 3.2***Key Temperatures from Thermal Analysis of Silk-Model Drug Fibers and Films*

Sample	Fiber		Film		
	Glass transition $T_G/^\circ\text{C}$	Major degradation $T_D/^\circ\text{C}$	Glass transition $T_{G1}/^\circ\text{C}$	Glass transition $T_{G2}/^\circ\text{C}$	Major degradation $T_D/^\circ\text{C}$
Pure silk	175	299	36	182	286
Alcian blue	N/A	298	48	N/A	292
Indigo carmine	N/A	302	64	N/A	302

Sample	Fiber		Film		
	Glass transition T <sub>G</sub> /°C	Major degradation T <sub>D</sub> /°C		Glass transition T <sub>G</sub> /°C	Major degradation T <sub>D</sub> /°C
Rifampin	N/A	301	54	N/A	297
Crystal violet	179	299	41	177	291
Rhodamine B	183	306	39	N/A	283

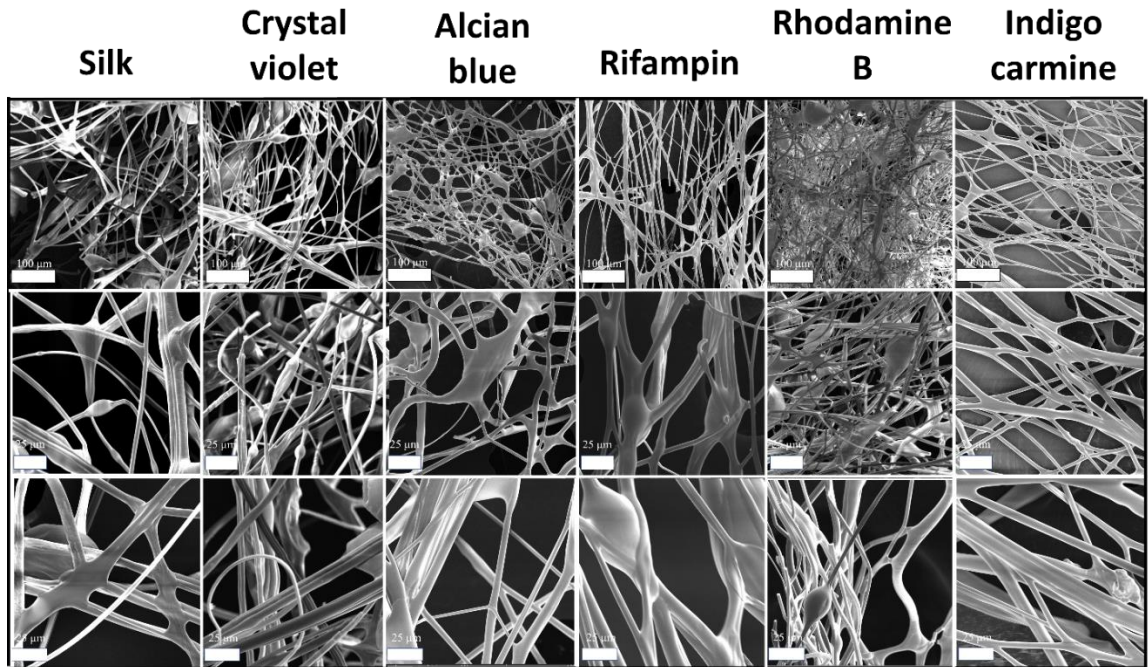
*Note.* Values obtained from DSC; Temperatures recorded in the middle of the curve for changes in heat flow (middle degradation) or heat capacity.

### ***3.3.3 Morphology Discussion***

SEM images were used to study the morphology of air-spun silk fibers and the effects of model drugs. The SEM images for silk fibers are pictured in Figure 3.8 for both pure silk fibers and model drug-embedded fibers at 100, 500, and 1000x magnification. Within all images, the fiber networks remain porous. Some aggregates of the model drugs are visible, but most of the network remains unaffected in its porosity by the addition of the model drugs. Based on this, the addition of model drugs at low weight percentages allows the fibers to maintain the beneficial morphology that makes fibrous materials valuable drug delivery vehicles. Further analysis was then done using ImageJ to measure the average diameters of the fibers. In all samples, with or without model drugs, the fiber diameters typically ranged from 4-9  $\mu\text{m}$ . There are also some small, nanofiber scale fibers within the microfibers, giving the silk fiber biomaterials a micro-nanofiber morphology.

**Figure 3.8**

*SEM Images of Silk-Model Drug Fibers*



*Note.* First row scale bars are 100  $\mu\text{m}$ . Second and third row scale bars are 25  $\mu\text{m}$ .

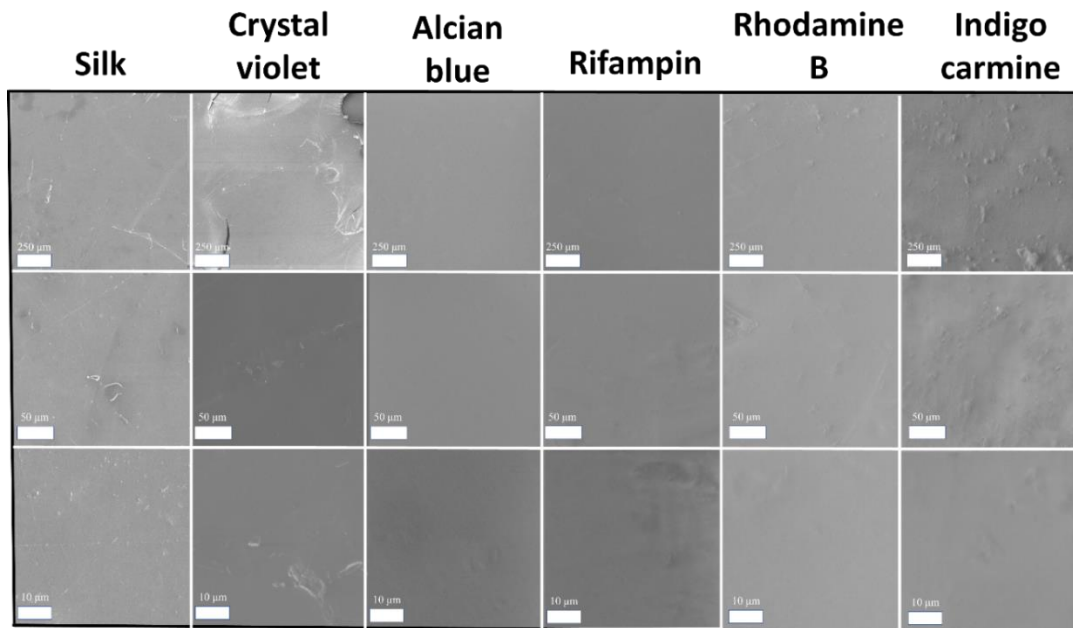
A similar analysis was also done on silk films. SEM images of the film surfaces were taken at 100, 500, and 2000x magnification (Figure 3.9). In all samples, there are few, if any, aggregates of the model drugs visible. The films show a smooth surface with even topography. Indigo carmine-embedded films showed the roughest topography, which was also the case in other studies of indigo carmine-embedded films<sup>8</sup>. Since indigo carmine is the only anionic model drug used, there may be electrostatic interactions during fabrication that influence the surface roughness of the films. Despite



this, the films are still fairly smooth, which would allow them to be used as effective drug delivery vehicles.

**Figure 3.9**

*SEM Images of Silk-Model Drug Thin Films*



*Note.* Scale bars from top to bottom row: 250  $\mu\text{m}$ , 50  $\mu\text{m}$ , 10  $\mu\text{m}$ .

### 3.3.4 Drug Release Testing

Because of the interesting protein-drug interactions seen in the FTIR and thermal analysis, plus the insignificant impact of model drugs on fiber morphology, a drug release test was conducted to see if these interactions also influenced the release kinetics of the

model drugs from the biomaterials. The model drugs chosen were used because of their varying size, weight, hydrophobicity, charge, and water solubility (Table 1) in addition to their similarity to the pharmaceuticals on the market today. A few of the molecules used also have historical significance in medicine. Rifampin, for example, was previously used to treat tuberculosis<sup>185</sup> and has recently been a potential therapeutic for atopic dermatitis<sup>186</sup>. Rifampin also exhibits anti-bacterial and anti-fungal activity, as does crystal violet<sup>187, 188</sup>. While oral delivery is the most common and easiest method of administration for most patients, rifampin is discouraged for oral use due to frequent off-target effects<sup>189-191</sup>. This can be avoided by using more localized deliver methods, including topical delivery. Here, silk fibers can provide a mat for rifampin to be delivered in a form similar to a bandage. Each of the model drugs used in this study also absorb light in the UV-visible spectrum, which allows for easy quantification of its release from the materials in an aqueous solution. The kinetics of model drug release was compared between 1D fiber geometry and 2D film geometry by using a two-sample T-test with an alpha significance level of 0.05.

The normalized release profiles of silk fibers and films embedded with model drugs are depicted in Figure 3.10a and Figure 3.10b, respectively. Normalization was performed with the maximum assumed to be the amount of drug released at 96 h; beyond this, there was not a significant release of the drugs. Since the release study was conducted in deionized water, the hydrophobicity of the model drugs played a large role in the trends seen. Rifampin, which is highly hydrophilic with a log P of -9.7, releases from both fiber and film samples nearly immediately (90%+ in 15 minutes). Despite this,

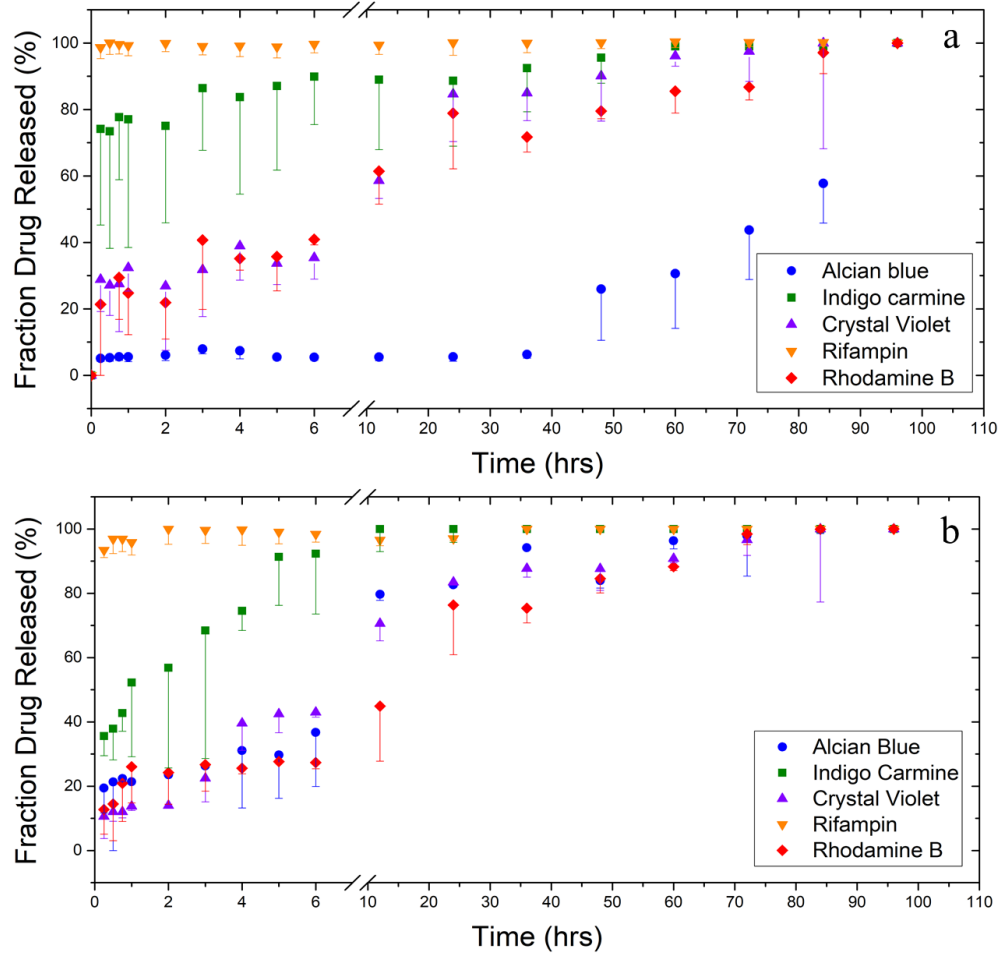
there is still a significant difference in release speeds because of the differing geometry that causes silk films to retain rifampin for a slightly longer amount of time ( $P=0.013$ ). This may be due to the large surface-area-to-volume ratio of the fiber samples exposing the surface of the fibers to more water than the surface of the films. This allows for enhanced mass transfer<sup>131</sup>, giving rifampin a quicker release from fiber samples than film samples. All other model drugs have a hydrophobic character, with indigo carmine having the lowest hydrophobic character ( $\log P = 1.01$ ). This low hydrophobic character caused indigo carmine to have the second quickest release out of the set of model drugs, but there was no significant difference in release speeds between the fibers and the films ( $P=0.072$ ). Regardless, indigo carmine is retained by the silk fibers and films much better; films retain the drug for 12 h and fibers for 60 h.

Crystal violet, rhodamine B, and alcian blue all have a much more sustained release. Crystal violet and rhodamine B have similar release profiles, which is sensible given their similar  $\log P$  values of 1.4 and 1.95, respectively. Like the indigo carmine-embedded samples, rhodamine B and crystal violet also have comparable release kinetics regardless of the biomaterial geometry. For crystal violet, the  $P$  value between films and fibers is 0.101 and for rhodamine B the  $P$  value is 0.085. Both crystal violet and rhodamine B are retained within the biomaterial for at least 12 h, and then see a slower release from the biomaterial while maintaining a continuous and relatively linear profile until all of the drug is released.

Alcian blue showed the slowest release out of this set of model drugs. This fits the hydrophobicity trend since alcian blue has a log P of 2.77. In addition, alcian blue is by far the largest, heaviest molecule which gives it the lowest water solubility. Statistical analysis showed that the biomaterial geometry had the strongest effect on release kinetics for alcian blue (P=0.00). In fiber samples, alcian blue had a slow, controlled release from the fiber network; 93% of alcian blue was retained over 36 h in silk fibers, but silk films release 19% of their embedded alcian blue in only 15 minutes. After 36 h, however, alcian blue does have an increase in its release speed from the silk fibers. This can be attributed to drug-drug interactions<sup>36</sup> where alcian blue interacts with itself to resist detachment from the silk fibers and dissolution into water. These interactions combined with the low solubility of the drug (1 mg/mL at 25 °C<sup>8</sup>) cause a slow release of alcian blue, especially early in the study when there are plenty of alcian blue molecules to interact with each other. The hydrophobic effect, which assist silk in its self-assembly through preferential folding of its hydrophobic amino acids, could also help slow the release of alcian blue in fibers where the porous geometry allows model drugs to better interact with the protein structure. Further evidence of this claim is given by the results of the post-soak FTIR spectrum (Figure 3.2c). In this analysis, there was the lowest shift towards intermolecular  $\beta$ -sheets compared to any of the other drugs. This implies that the size and hydrophobicity of alcian blue inhibited the ability of silk to self-assemble into intermolecular  $\beta$ -sheets while also protecting itself from water. Because silk films did not have these same interactions in the protein structure (Figure 3.3c), alcian blue was less protected by the silk protein structure and released from the films quicker than the fibers.

**Figure 3.10**

*Release Profiles from Silk-Model Drug Fibers and Films*



*Note.* Normalized release profiles of various model drugs from silk (a) fibers and (b) thin films. Error bars represent standard deviation.

**Table 3.3***Statistical Values from Model Drug Release*

<b>Model Drug</b>	<b>Pearson Correlation</b>	<b>T-Stat</b>	<b>P(T≤t)</b>
Alcian blue	0.645	-5.781	0.00
Indigo carmine	0.914	1.929	0.072
Rifampin	0.488	2.792	0.013
Crystal violet	0.971	1.740	0.101
Rhodamine B	0.979	1.839	0.085

*Note.* All probabilities are compared to a two tailed t Critical of 2.120 and an alpha significance level of 0.05.

### ***3.3.5 Mechanism of Interaction***

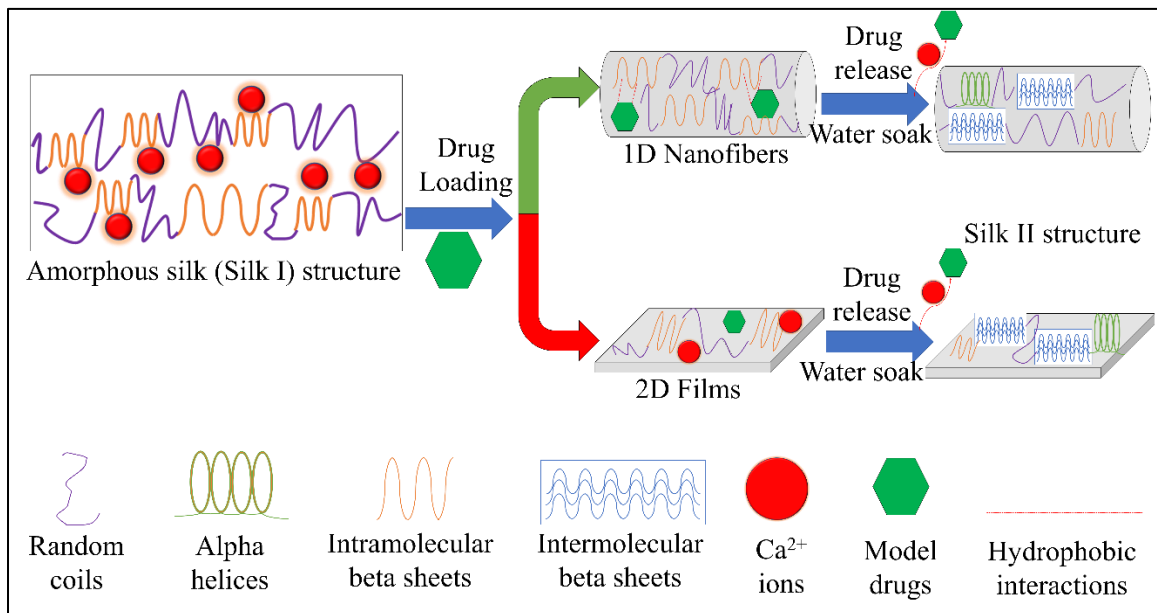
Silk-based fibrous materials provide a potential platform for the delivery of therapeutic molecules based on the interactions seen in this study. Specifically, the porous 1D geometry of fibers, when combined with the physicochemical properties of the therapeutic, provide a means of fine-tuning the release kinetics of the therapeutic from

the fiber network. While the flat 2D geometry of silk films makes it harder for therapeutic molecules to interact with the silk protein structure, there are still differences in release kinetics compared to silk fibers, which make them another platform for specific drug delivery applications. Regardless, silk fibers can also provide additional benefits over silk films. The 1D geometry of the fibers allows molecules to infiltrate the porous network and interact with the self-assembling silk protein, which provides thermal protection (rifampin, rhodamine B, indigo carmine) or slows their release from the fibers (alcian blue). These protective interactions are comparable to the hydrophobic effect. As silk proteins inside the biomaterials self-assemble into intermolecular  $\beta$ -sheets, especially in an aqueous environment, the chemical and physical properties of the embedded drugs can influence this folding. As a result, understanding the biochemical and biophysical interactions between a molecule and the protein structure can fine tune mechanical and thermal properties of the biomaterial as well as the release kinetics of the molecule from the biomaterial. In the flat, nonporous 2D geometry of silk films, model drugs are not able to interact with the protein structure as well as in the fiber networks. This prevents drug-protein interactions, resulting in lower thermal stability and less control of the release kinetics for the embedded silk films. These drug-protein interactions and their effects on the silk protein structure are illustrated in Figure 3.11. Other studies of silk-based drug delivery vehicles have shown similar results where the  $\beta$ -sheets of silk II were important in regulating the release kinetics of embedded drugs<sup>32, 174</sup>. . A major takeaway from this study is that diffusion and mass transfer properties alone not the only properties that dictate model drug release kinetics. In a protein-based drug delivery vehicle, the

biochemical and biophysical interactions between the protein structure and the choice of therapeutic molecule are also important to understand in order to create specifically-tuned drug delivery vehicles for a wide range of applications.

**Figure 3.11**

*Mechanism of Interaction*



*Note.* Porous 1D fiber networks allow for the integration of model drugs, which then influence the self-folding behavior of silk protein. In flat 2D films, model drugs are unable to interact in the same way. As a result, fibers are able to protect embedded model drugs from thermal degradation and slow the release of the molecules from its structure. In thin films, the drugs are more susceptible to thermal degradation and there is less control over their release.



### 3.4 Conclusions

Within this study, air-spraying was used as a novel nano-microfiber creation method to create model-drug embedded silk fibers with high throughput without the need for a high voltage power source. Analysis of the air-spun fibers showed that the porous 1D geometry created a network for model drugs to interact with the silk protein structure in order to tailor the release kinetics of the drugs and provide thermal protection. The release kinetics followed a trend with the hydrophobicity of the model drugs, which highlighted the importance of biophysical and biochemical properties when designing a protein-based drug delivery vehicle. This study found that the hydrophobicity of the model drugs impacted the self-assembly of silk protein in a matter similar to how the hydrophobic effect helps facilitate the native folding of silk. While these interactions were common and measurable within the fiber samples, the flat, 2D geometry of the films prevented these same interactions. As a result, embedded silk films had lower control over the release kinetics of the model drugs and lower thermal stability. By better understanding the biophysical and biochemical interactions between therapeutic molecules and the protein structure of silk biomaterials, it will be possible to create fine-tuned drug delivery vehicles with specific material properties and release kinetics for specific applications.

## Chapter 4

### Conclusion

The overall goal of this project was to showcase the potential of protein-based biomaterials for drug delivery applications. Chapter 1 gave an overview of proteins, polysaccharides, and their composites that are commonly used in biomaterials research. The potential of these biomacromolecules was then discussed, especially with respect to drug delivery applications. This study focused on thin films and nanofibers because of their ease of fabrication and differing geometries (1D nanofibers vs. 2D films). Chapter 2 then explored the potential of corn zein thin films and nanofibers for the delivery of the topical therapeutic sodium citrate. Formic acid was used to dissolve a large amount of zein and up to 30 wt% sodium citrate into the same solution, which was then cast into 2D films or spun into 1D nanofibers using a novel air-spraying method. Air-spraying proved to be an easy, safe, and effective method for producing a large amount of nanofibers in a short amount of time compared to conventional methods like electrospinning. Additionally, the fabrication method was proven to be safe by biocompatibility assays and MTT assays with a human cell line. Most notably, this study revealed that sodium citrate could interact with the protein structure of corn zein nanofibers to shift the structure from a less stable random coil structure towards a more stable alpha helical structure based on FTIR and DSC analysis. In the 2D geometry of corn zein films, however, this same shift did not occur, indicating that biomaterial geometry is a critical factor in fine-tuning the release of sodium citrate from the biomaterial structure. A

statistical analysis confirmed a significantly different release profile between fibers and films for the same wt% of sodium citrate except for 30 wt% sodium citrate, which was revealed to lose its porous geometry in SEM analysis, thus likening its release to that of the 2D films. This study showed that corn zein can interact with therapeutic molecules to fine-tune the release of the therapeutics from them in a porous, 1D nanofiber network, but not in 2D films. Future studies with corn zein should focus on the biophysical and biochemical interactions in differing biomaterial geometries.

After the success of corn zein nanofibers, a parallel study was conducted using *Bombyx mori* silk and a variety of model drugs. Five different model drugs of varying weight, hydrophobicity, charge, and solubility were chosen to represent a range of pharmaceuticals in use today. Morphology and drug release studies showed similar results to the zein study; in the 1D, porous geometry of nanofibers, the model drugs were able to shift the protein structure of the silk nanofibers slightly in order to change their crystallinity (beta sheet content). Hydrophobic drugs were able to cause a bigger shift towards intermolecular beta sheets, indicating that the hydrophobic effect and protein self-folding mechanisms likely had influence. The more hydrophobic drugs were able to be folded away in the protein structure, protecting them from thermal degradation and slowing their release from the nanofiber mats. In 2D silk films, however, this shift in protein structure did not occur, resulting in less control of the release of model drugs from the film structure. While nanofibers showed an obvious relationship between hydrophobicity and release speed, this was not the case in films.

The results of both studies indicate that diffusion is not the only driving force in the release of therapeutic molecules from biomaterials. The biophysical and biochemical interactions between therapeutic molecules and the protein backbone of biomaterials plays an equally important role in tailoring the release profile of the therapeutics. Because of this, the physicochemical nature of the therapeutics and the biomaterial backbone are important to understand when designing a drug delivery vehicle, as is the geometry of the biomaterial. With a better understanding of these mechanisms, new fabrication techniques can be created to specifically match up therapeutic molecules with protein structures and biomaterial geometries to fine-tune the release profile on a case-by-case basis.

## References

1. David, K., Advances and challenges with fibrous protein biomaterial designs. *Frontiers in Bioengineering and Biotechnology* **2016**, *4*.
2. Toita, S.; Morimoto, N.; Akiyoshi, K., Functional cycloamylose as a polysaccharide-based biomaterial: application in a gene delivery system. *Biomacromolecules* **2010**, *11* (2), 397-401.
3. Mohan, T.; Čas, A.; Bračić, M.; Plohl, O.; Vesel, A.; Rupnik, M.; Zemljič, L. F.; Rebol, J., Highly Protein Repellent and Antiadhesive Polysaccharide Biomaterial Coating for Urinary Catheter Applications. *ACS Biomaterials Science and Engineering* **2019**, *5* (11), 5825-5832.
4. *Polysaccharide Based Graft Copolymers*. 1st ed. 2013. ed.; Springer Berlin Heidelberg: Berlin, Heidelberg, 2013.
5. *Protein-based Engineered Nanostructures*. 1st ed. 2016. ed.; Springer International Publishing: Cham, 2016.
6. Leipzig, N. D.; Wylie, R. G.; Kim, H.; Shoichet, M. S., Differentiation of neural stem cells in three-dimensional growth factor-immobilized chitosan hydrogel scaffolds. *Biomaterials* **2011**, *32* (1), 57-64.
7. Hayden, R. S.; Quinn, K. P.; Alonzo, C. A.; Georgakoudi, I.; Kaplan, D. L., Quantitative characterization of mineralized silk film remodeling during long-term osteoblast–osteoclast co-culture. *Biomaterials* **2014**, *35* (12), 3794-3802.
8. DeFrates, K.; Markiewicz, T.; Xue, Y.; Callaway, K.; Gough, C.; Moore, R.; Bessette, K.; Mou, X.; Hu, X., Air-jet spinning corn zein protein nanofibers for drug delivery: Effect of biomaterial structure and shape on release properties. *Mater. Sci. Eng. C* **2021**, *118*, 111419.
9. Yewale, C.; Baradia, D.; Vhora, I.; Misra, A., Proteins: emerging carrier for delivery of cancer therapeutics. *Expert Opinion on Drug Delivery* **2013**, *10* (10), 1429-1448.
10. Mottaghitlab, F.; Farokhi, M.; Shokrgozar, M. A.; Atyabi, F.; Hosseinkhani, H., Silk fibroin nanoparticle as a novel drug delivery system. *J. Controlled Release* **2015**, *206*, 161-176.
11. Han, Y.-L.; Xu, Q.; Lu, Z.; Wang, J.-Y., Cell adhesion on zein films under shear stress field. *Colloids and Surfaces B: Biointerfaces* **2013**, *111*, 479-485.
12. Reeves, A. R. D.; Spiller, K. L.; Freytes, D. O.; Vunjak-Novakovic, G.; Kaplan, D. L., Controlled release of cytokines using silk-biomaterials for macrophage polarization. *Biomaterials* **2015**, *73*, 272-283.

13. Sutherland, T. D.; Young, J. H.; Weisman, S.; Hayashi, C. Y.; Merritt, D. J., Insect silk: one name, many materials. *Annu Rev Entomol* **2010**, *55*, 171-88.
14. Rudall, K. M.; Kenchington, W., Arthropod Silks: The Problem of Fibrous Proteins in Animal Tissues. *Annual Review of Entomology* **1971**, *16* (1), 73-96.
15. Florkin, M., *Comparative Biochemistry V4: A Comprehensive Treatise*. Elsevier Science: 2012.
16. Extracellular fibrous proteins: the silks. *Comprehensive Biochem* **1968**, *26* (B), 475-558.
17. Dhyani, V.; Singh, N., Controlling the cell adhesion property of silk films by graft polymerization. *ACS Appl. Mater. Interfaces* **2014**, *6* (7), 5005-5011.
18. Hu, X.; Raja, W. K.; An, B.; Tokareva, O.; Cebe, P.; Kaplan, D. L., Stability of Silk and Collagen Protein Materials in Space.
19. Slotta, U.; Tammer, M.; Kremer, F.; Koelsch, P.; Scheibel, T., Structural Analysis of Spider Silk Films. *Supramolecular Chemistry: Special Issue on Supramolecular Biochemical Assemblies* **2006**, *18* (5), 465-471.
20. Dinis, T. M.; Vidal, G.; Jose, R. R.; Vigneron, P.; Bresson, D.; Fitzpatrick, V.; Marin, F.; Kaplan, D. L.; Egles, C., Complementary effects of two growth factors in multifunctionalized silk nanofibers for nerve reconstruction. *PloS one* **2014**, *9* (10), e109770-e109770.
21. Cohen-Karni, T.; Jeong, K. J.; Tsui, J. H.; Reznor, G.; Mustata, M.; Wanunu, M.; Graham, A.; Marks, C.; Bell, D. C.; Langer, R.; Kohane, D. S., Nanocomposite gold-silk nanofibers. *Nano Lett.* **2012**, *12* (10), 5403-5406.
22. Wang, C.; Wu, S.; Jian, M.; Xie, J.; Xu, L.; Yang, X.; Zheng, Q.; Zhang, Y., Silk nanofibers as high efficient and lightweight air filter. *Nano Res.* **2016**, *9* (9), 2590-2597.
23. Wenk, E.; Merkle, H. P.; Meinel, L., Silk fibroin as a vehicle for drug delivery applications. *J. Controlled Release* **2011**, *150* (2), 128-141.
24. Asakura, T.; Miller, T., *Biotechnology of Silk*. Springer Netherlands: 2013.
25. Chun, H. J.; Park, K.; Kim, C. H.; Khang, G., *Novel Biomaterials for Regenerative Medicine*. Springer Singapore: 2018.
26. Dae-Hyeong, K.; Jonathan, V.; Jason, J. A.; Jianliang, X.; Leif, V.; Yun-Soung, K.; Justin, A. B.; Bruce, P.; Eric, S. F.; Diego, C.; David, L. K.; Fiorenzo, G. O.; Yonggang, H.; Keh-Chih, H.; Mitchell, R. Z.; Brian, L.; John, A. R., Dissolvable films of silk fibroin for ultrathin conformal bio-integrated electronics. *Nature Materials* **2010**, *9* (6), 511.

27. Kim, D.-H.; Kim, Y.-S.; Amsden, J.; Panilaitis, B.; Kaplan, D. L.; Omenetto, F. G.; Zakin, M. R.; Rogers, J. A., Silicon electronics on silk as a path to bioresorbable, implantable devices. *Appl. Phys. Lett.* **2009**, *95* (13), 133701.
28. Yin, Z.; Jian, M.; Wang, C.; Xia, K.; Liu, Z.; Wang, Q.; Zhang, M.; Wang, H.; Liang, X.; Liang, X.; Long, Y.; Yu, X.; Zhang, Y., Splash-Resistant and Light-Weight Silk-Sheathed Wires for Textile Electronics. *Nano Lett.* **2018**, *18* (11), 7085.
29. Fox, D.; Fylstra, P.; Hanley, M.; Henderson, W. A.; Trulove, P. C.; Bellayer, S.; Gilman, J.; De Long, H. C. In *The Preparation and Characterization of Bombyx Mori Silk Nanocomposites Using Ionic Liquids*, ECS Transactions, ECS: 2007.
30. Phillips, D. M.; Drummy, L. F.; Naik, R. R.; Long, H. C. D.; Fox, D. M.; Trulove, P. C.; Mantz, R. A., Regenerated silk fiber wet spinning from an ionic liquid solution. *J. Mater. Chem.* **2005**, *15* (39), 4206-4208.
31. Jiang, F.; Liu, K.; Zhao, M.; Tao, X.; Hu, X.; Lu, S., Tunable High-Molecular-Weight Silk Fibroin Polypeptide Materials: Fabrication and Self-Assembly Mechanism. *ACS Applied Bio Materials* **2020**, *3* (5), 3248-3259.
32. Wei, Q. N.; Huang, A. M.; Ma, L.; Huang, Z.; Huang, X.; Qiang, P. P.; Gong, Z. P.; Zhang, L., Structure regulation of silk fibroin films for controlled drug release. *J. Appl. Polym. Sci.* **2012**, *125* (S2), E477-E484.
33. Paraman, I.; Lamsal, B. P., Recovery and Characterization of  $\alpha$ -Zein from Corn Fermentation Coproducts. *J. Agric. Food. Chem.* **2011**, *59* (7), 3071-3077.
34. Kasaai, M. R., Zein and zein -based nano-materials for food and nutrition applications: A review. *Trends in food science & technology* **2018**, *79*, 184-197.
35. Guo, Y.; Liu, Z.; An, H.; Li, M.; Hu, J., Nano-structure and properties of maize zein studied by atomic force microscopy. *Journal of Cereal Science* **2005**, *41* (3), 277-281.
36. Gough, C. R.; Bessette, K.; Xue, Y.; Mou, X.; Hu, X., Air-Jet Spun Corn Zein Nanofibers and Thin Films with Topical Drug for Medical Applications. *Int. J. Mol. Sci.* **2020**, *21* (16), 5780.
37. Erickson, D. P.; Ozturk, O. K.; Selling, G.; Chen, F.; Campanella, O. H.; Hamaker, B. R., Corn zein undergoes conformational changes to higher  $\beta$ -sheet content during its self-assembly in an increasingly hydrophilic solvent. *Int. J. Biol. Macromol.* **2020**, *157*, 232-239.
38. Wang, Y.; Padua, G. W., Nanoscale Characterization of Zein Self-Assembly. *Langmuir* **2012**, *28* (5), 2429-2435.
39. Zhang, Y.; Li, W.-Y.; Lan, R.; Wang, J.-Y., Quality Monitoring of Porous Zein Scaffolds: A Novel Biomaterial. *Engineering* **2017**, *3* (1), 130-135.

40. Zein: a potential biomaterial for tissue engineering: Tissue engineering. *Mater. Today* **2004**, 7 (7-8), 24-24.
41. Lee, S.; Alwahab, N. S. A.; Moazzam, Z. M., Zein-based oral drug delivery system targeting activated macrophages. *Int. J. Pharm.* **2013**, 454 (1), 388-393.
42. Shi, K.; Huang, Y.; Yu, H.; Lee, T.-C.; Huang, Q., Reducing the brittleness of zein films through chemical modification. *J. Agric. Food. Chem.* **2011**, 59 (1), 56.
43. Hudson, S. M., The Spinning of Silk-like Proteins Into Fibers. In *Protein-Based Materials*, McGrath, K.; Kaplan, D., Eds. Birkhäuser Boston: Boston, MA, 1997; pp 313-337.
44. Ptiček Siročić, A., Characterization of Casein Fractions – Comparison of Commercial Casein and Casein Extracted from Cow's Milk. *Chem. Biochem. Eng. Q.* **2017**, 30 (4), 501-509.
45. Elzoghby, A. O.; Abo El-Fotoh, W. S.; Elgindy, N. A., Casein-based formulations as promising controlled release drug delivery systems. *J. Controlled Release* **2011**, 153 (3), 206-216.
46. Wang, H.-J.; Di, L.; Ren, Q.-S.; Wang, J.-Y., Applications and Degradation of Proteins Used as Tissue Engineering Materials. *Materials* **2009**, 2 (2), 613-635.
47. Ellis, B.; Smith, R., *Polymers: A Property Database, Second Edition*. CRC Press: 2008.
48. Wool, R.; Sun, X. S., *Bio-Based Polymers and Composites*. Elsevier Science: 2011.
49. Liu, X.; Souzandeh, H.; Zheng, Y.; Xie, Y.; Zhong, W.-H.; Wang, C., Soy protein isolate/bacterial cellulose composite membranes for high efficiency particulate air filtration. *Compos. Sci. Technol.* **2017**, 138, 124-133.
50. Kang, H.-J.; Kim, S.-J.; You, Y.-S.; Lacroix, M.; Han, J., Inhibitory effect of soy protein coating formulations on walnut (*Juglans regia* L.) kernels against lipid oxidation. *LWT - Food Science and Technology* **2013**, 51 (1), 393-396.
51. Chuysinuan, P.; Pongsuk, C.; Lirdprapamongkol, K.; Techasakul, S.; Svasti, J.; Nooeaid, P., Enhanced Structural Stability and Controlled Drug Release of Hydrophilic Antibiotic-Loaded Alginate/Soy Protein Isolate Core-Sheath Fibers for Tissue Engineering Applications. *Fibers Polym.* **2019**, 20 (1), 1-10.
52. Peles, Z.; Binderman, I.; Berdicevsky, I.; Zilberman, M., Soy protein films for wound-healing applications: antibiotic release, bacterial inhibition and cellular response. *Journal of Tissue Engineering and Regenerative Medicine* **2013**, 7 (5), 401-412.



53. Noshad, M.; Mohebbi, M.; Koocheki, A.; Shahidi, F., Microencapsulation of vanillin by spray drying using soy protein isolate–maltodextrin as wall material. *Flavour and Fragrance Journal* **2015**, *30* (5), 387-391.
54. Lee, C.-H.; Yun, Y. J.; Cho, H.; Lee, K. S.; Park, M.; Kim, H. Y.; Son, D. I., Environment-friendly, durable, electro-conductive, and highly transparent heaters based on silver nanowire functionalized keratin nanofiber textiles. *Journal of Materials Chemistry C* **2018**, *6* (29), 7847-7854.
55. Aluigi, A.; Corbellini, A.; Rombaldoni, F.; Mazzuchetti, G., Wool-derived keratin nanofiber membranes for dynamic adsorption of heavy-metal ions from aqueous solutions. *Textile Research Journal* **2013**, *83* (15), 1574-1586.
56. Murrell, D. F.; Trisnowati, N.; Miyakis, S.; Paller, A. S., The Yin and the Yang of Keratin Amino Acid Substitutions and Epidermolysis Bullosa Simplex. *Journal of Investigative Dermatology* **2011**, *131* (9), 1787-1790.
57. Dullaart, R.; Mousquès, J. o., *Keratin structure, properties, and applications*. Nova Publishers: New York, 2012.
58. Feng, Y.; Borrelli, M.; Meyer-Ter-Vehn, T.; Reichl, S.; Schrader, S.; Geerling, G., Epithelial Wound Healing on Keratin Film, Amniotic Membrane and Polystyrene In Vitro. *Current Eye Research* **2014**, *39* (6), 561-570.
59. Cui, L.; Gong, J.; Fan, X.; Wang, P.; Wang, Q.; Qiu, Y., Transglutaminase-modified wool keratin film and its potential application in tissue engineering. *Engineering in Life Sciences* **2013**, *13* (2), 149-155.
60. Lusiana; Reichl, S.; Müller-Goymann, C. C., Keratin film made of human hair as a nail plate model for studying drug permeation. *European Journal of Pharmaceutics and Biopharmaceutics* **2011**, *78* (3), 432-440.
61. Lin, K.; Zhang, D.; Macedo, M. H.; Cui, W.; Sarmiento, B.; Shen, G., Advanced Collagen-Based Biomaterials for Regenerative Biomedicine. *Adv. Funct. Mater.* **2019**, *29* (3), 1804943-n/a.
62. Brennan, A. B.; Kirschner, C. M.; Kirschner, C. M., *Bio-Inspired Materials for Biomedical Engineering*. John Wiley & Sons, Incorporated: Somerset, UNITED STATES, 2014.
63. Meng, Z.; Zheng, X.; Tang, K.; Liu, J.; Ma, Z.; Zhao, Q., Dissolution and regeneration of collagen fibers using ionic liquid. *Int. J. Biol. Macromol.* **2012**, *51* (4), 440-448.
64. Wise, S. G.; Weiss, A. S., Tropoelastin. *The International Journal of Biochemistry & Cell Biology* **2009**, *41* (3), 494-497.

65. Csiszar, K., Lysyl oxidases: A novel multifunctional amine oxidase family. In *Progress in Nucleic Acid Research and Molecular Biology*, Academic Press: 2001; Vol. 70, pp 1-32.
66. Waterhouse, A.; Wise, S. G.; Ng, M. K. C.; Weiss, A. S., Elastin as a Nonthrombogenic Biomaterial. *Tissue Engineering Part B: Reviews* **2011**, *17* (2), 93-99.
67. Daamen, W. F.; Veerkamp, J. H.; van Hest, J. C. M.; van Kuppevelt, T. H., Elastin as a biomaterial for tissue engineering. *Biomaterials* **2007**, *28* (30), 4378-4398.
68. Reguera, J.; Fahmi, A.; Moriarty, P.; Girotti, A.; Rodríguez-Cabello, J. C., Nanopore Formation by Self-Assembly of the Model Genetically Engineered Elastin-like Polymer [(VPGVG)<sub>2</sub>(VPGEG)(VPGVG)<sub>2</sub>]<sub>15</sub>. *Journal of the American Chemical Society* **2004**, *126* (41), 13212-13213.
69. Bellingham, C. M.; Lillie, M. A.; Gosline, J. M.; Wright, G. M.; Starcher, B. C.; Bailey, A. J.; Woodhouse, K. A.; Keeley, F. W., Recombinant human elastin polypeptides self-assemble into biomaterials with elastin-like properties. *Biopolymers* **2003**, *70* (4), 445-455.
70. Herrero-Vanrell, R.; Rincon Ac Fau - Alonso, M.; Alonso M Fau - Reboto, V.; Reboto V Fau - Molina-Martinez, I. T.; Molina-Martinez It Fau - Rodriguez-Cabello, J. C.; Rodriguez-Cabello, J. C., Self-assembled particles of an elastin-like polymer as vehicles for controlled drug release. *J Control Release* **2005**, *102*(1) (0168-3659 (Print)).
71. Mithieux, S. M.; Rasko Je Fau - Weiss, A. S.; Weiss, A. S., Synthetic elastin hydrogels derived from massive elastic assemblies of self-organized human protein monomers. *Biomaterials* **2004**, *25*(20) (0142-9612 (Print)).
72. Wright, E. R.; McMillan, R. A.; Cooper, A.; Apkarian, R. P.; Conticello, V. P., Thermoplastic Elastomer Hydrogels via Self-Assembly of an Elastin-Mimetic Triblock Polypeptide. *Adv. Funct. Mater.* **2002**, *12* (2), 149-154.
73. Desai, H. E., Synthesis and Structural Characterization of Reflectin Proteins. North Georgia, C.; State Univ, D., Eds. 2012.
74. Tao, A. R.; Demartini, D. G.; Izumi, M.; Sweeney, A. M.; Holt, A. L.; Morse, D. E., The role of protein assembly in dynamically tunable bio-optical tissues. *Biomaterials* **2010**, *31* (5), 793-801.
75. Arulmoli, J., Scaffolds for Neural Stem Cell Tissue Engineering. **2016**.
76. Kramer, R. M.; Crookes-Goodson, W. J.; Naik, R. R., The self-organizing properties of squid reflectin protein. *Nature Materials* **2007**, *6* (7), 533-538.
77. Shin, Y. M.; Hohman, M. M.; Brenner, M. P.; Rutledge, G. C., Experimental characterization of electrospinning: the electrically forced jet and instabilities. *Polymer* **2001**, *42* (25), 09955-09967.

78. Lyons, J.; Li, C.; Ko, F., Melt-electrospinning part I: processing parameters and geometric properties. *Polymer* **2004**, *45* (22), 7597-7603.
79. Chronakis, I. S., Novel nanocomposites and nanoceramics based on polymer nanofibers using electrospinning process—A review. *J. Mater. Process. Technol.* **2005**, *167* (2), 283-293.
80. Love, S. A.; Popov, E.; Rybacki, K.; Hu, X.; Salas-de la Cruz, D., Facile treatment to fine-tune cellulose crystals in cellulose-silk biocomposites through hydrogen peroxide. *Int. J. Biol. Macromol.* **2020**, *147*, 569-575.
81. Blessing, B.; Trout, C.; Morales, A.; Rybacki, K.; Love, S. A.; Lamoureux, G.; O'Malley, S. M.; Hu, X.; Salas-de la Cruz, D., Morphology and ionic conductivity relationship in silk/cellulose biocomposites. *Polym. Int.* **2019**, *68* (9), 1580-1590.
82. Arai, T.; Freddi, G.; Innocenti, R.; Tsukada, M., Biodegradation of Bombyx mori silk fibroin fibers and films. *J. Appl. Polym. Sci.* **2004**, *91* (4), 2383-2390.
83. Lai, H. M.; Padua, G. W., Properties and Microstructure of Plasticized Zein Films. *Cereal Chem.* **1997**, *74* (6), 771-775.
84. Hueimmerich, D.; Slotta, U.; Scheibel, T., Processing and modification of films made from recombinant spider silk proteins. *Appl. Phys. A* **2006**, *82* (2), 219-222.
85. Li, R.; Wang, D., Preparation of regenerated wool keratin films from wool keratin-ionic liquid solutions. *J. Appl. Polym. Sci.* **2013**, *127* (4), 2648-2653.
86. Wang, F.; Wolf, N.; Rocks, E.-M.; Vuong, T.; Hu, X., Comparative studies of regenerated water-based Mori, Thai, Eri, Muga and Tussah silk fibroin films. *J. Therm. Anal. Calorim.* **2015**, *122* (3), 1069-1076.
87. Xue, Y.; Jao, D.; Hu, W.; Hu, X., Silk-silk blend materials: A comparative study of Mori-Tussah, Mori-Muga, Mori-Eri, and Mori-Thai silk films. *J. Therm. Anal. Calorim.* **2017**, *127* (1), 915-921.
88. Wang, F.; Yu, H.-y.; Gu, Z.-G.; Si, L.; Liu, Q.-c.; Hu, X., Impact of calcium chloride concentration on structure and thermal property of Thai silk fibroin films. *J. Therm. Anal. Calorim.* **2017**, *130* (2), 851-859.
89. Zhang, H.; Mittal, G., Biodegradable protein-based films from plant resources: A review. *Environmental progress & sustainable energy* **2010**, *29* (2), 203-220.
90. Liu, Q.; Wang, F.; Li, Y.; Yu, H.; Gu, Z., Comparative studies of structure, thermal decomposition mechanism and thermodynamic parameters of two kinds of silk fibroin films. *SCIENTIA SINICA Chimica* **2019**, *49*, 1014-1029.
91. Huot, A.; Lefèvre, T.; Rioux-Dubé, J.-F.; Paquet-Mercier, F.; Nault, A.-P.; Auger, M.; Pézolet, M., Effect of Mechanical Deformation on the Structure of

Regenerated Bombyx mori Silk Fibroin Films as Revealed Using Raman and Infrared Spectroscopy. *Appl. Spectrosc.* **2015**, 69 (6), 689-698.

92. Yudin, V. E.; Dobrovolskaya, I. P.; Neelov, I. M.; Dresvyanina, E. N.; Popryadukhin, P. V.; Ivan'kova, E. M.; Elokhovskii, V. Y.; Kasatkin, I. A.; Okrugin, B. M.; Morganti, P., Wet spinning of fibers made of chitosan and chitin nanofibrils. *Carbohydr. Polym.* **2014**, 108, 176-182.

93. DeFrates, K. G.; Moore, R.; Borgesi, J.; Lin, G.; Mulderig, T.; Beachley, V.; Hu, X., Protein-Based Fiber Materials in Medicine: A Review. *Nanomaterials (Basel, Switzerland)* **2018**, 8 (7), 457.

94. Grimmelsmann, N.; Grothe, T.; Homburg, S. V.; Ehrmann, A., Electrospinning and stabilization of chitosan nanofiber mats. Institute of Physics Publishing: 2017; Vol. 254.

95. Yao, C.; Li, X.; Song, T., Electrospinning and crosslinking of zein nanofiber mats. *J. Appl. Polym. Sci.* **2007**, 103 (1), 380-385.

96. Jiang, Q.; Yang, Y., Water-Stable Electrospun Zein Fibers for Potential Drug Delivery. *Journal of Biomaterials Science, Polymer Edition* **2011**, 22 (10), 1393-1408.

97. Huang, W.; Zou, T.; Li, S.; Jing, J.; Xia, X.; Liu, X., Drug-Loaded Zein Nanofibers Prepared Using a Modified Coaxial Electrospinning Process. *AAPS PharmSciTech* **2013**, 14 (2), 675-681.

98. Shen, X., Regeneration spider silk fiber based on ionic liquid and preparation method of regeneration spider silk fiber. 2015.

99. Lubasova D Fau - Netravali, A.; Netravali A Fau - Parker, J.; Parker J Fau - Ingel, B.; Ingel, B., Bacterial filtration efficiency of green soy protein based nanofiber air filter. *J. Nanosci. Nanotechnol.* **2014**, 14 (8), 4891-4898.

100. Liu, J.; Dunne, F. O.; Fan, X.; Fu, X.; Zhong, W.-H., A protein-functionalized microfiber/protein nanofiber Bi-layered air filter with synergistically enhanced filtration performance by a viable method. *Sep. Purif. Technol.* **2019**, 229, 115837.

101. Wang, C.; Wu, S.; Muqiang, J.; Xie, J.; Xu, L.; Yang, X.; Zheng, Q.; Zhang, Y., Silk nanofibers as high efficient and lightweight air filter. *Nano Res.* **2016**, 9 (9), 2590-2597.

102. Schiffman, J. D.; Schauer, C. L., One-Step Electrospinning of Cross-Linked Chitosan Fibers. *Biomacromolecules* **2007**, 8 (9), 2665-2667.

103. Magaz, A. n.; Roberts, A. D.; Faraji, S.; Nascimento, T. R. L.; Medeiros, E. S.; Zhang, W.; Greenhalgh, R. D.; Mautner, A.; Li, X.; Blaker, J. J., Porous, Aligned, and Biomimetic Fibers of Regenerated Silk Fibroin Produced by Solution Blow Spinning. *Biomacromolecules* **2018**, 19 (12), 4542-4553.

104. Chunya Wang, S. W. M. J. J. X. L. X. X. Y. Q. Z. Y. Z., Silk nanofibers as high efficient and lightweight air filter. *Nano Res.* **2016**, 9 (9), 2590-2597.
105. D. Lubasova, A. N. J. P. B. I., Bacterial Filtration Efficiency of Green Soy Protein Based Nanofiber Air Filter. *J. Nanosci. Nanotechnol.* **2014**, 14 (7), 4891-4898.
106. Fei Liu, R. J. A.-B. R. W. B.-S. C. T. G. W. D. F. W. C. B.-S. W. Y. G. M. G. T. H. M. F., Preparation of Zein Fibers Using Solution Blow Spinning Method. *J. Food Sci.* **2016**, 81 (12), 3015.
107. S J Lee, D. N. H. J. H. M. W. K. K. J. B. L. M. S. B. S. W. P. J. E. K., Electrospun chitosan nanofibers with controlled levels of silver nanoparticles. Preparation, characterization and antibacterial activity. *Carbohydr. Polym.* **2014**, 111, 530-537.
108. Kolbasov, A.; Sinha-Ray, S.; Jojode, A.; Hassan, M. A.; Brown, D.; Maze, B.; Pourdeyhimi, B.; Yarin, A. L., Industrial-Scale Solution Blowing of Soy Protein Nanofibers. *Ind. Eng. Chem. Res.* **2016**, 55 (1), 323-333.
109. Min, K.; Kim, S.; Kim, S., Silk protein nanofibers for highly efficient, eco-friendly, optically translucent, and multifunctional air filters. *Scientific Reports* **2018**, 8 (1), 9598.
110. Jin, J.; Lee, D.; Im, H.-G.; Han, Y. C.; Jeong, E. G.; Rolandi, M.; Choi, K. C.; Bae, B.-S., Chitin Nanofiber Transparent Paper for Flexible Green Electronics. *Adv. Mater.* **2016**, 28 (26), 5169-5175.
111. Paliwal, R.; Palakurthi, S., Zein in controlled drug delivery and tissue engineering. *J. Controlled Release* **2014**, 189, 108-122.
112. Kenawy, E.-R.; Abdel-Hay, F. I.; El-Newehy, M. H.; Wnek, G. E., Processing of polymer nanofibers through electrospinning as drug delivery systems. *Mater. Chem. Phys.* **2009**, 113 (1), 296-302.
113. Mahmood, H.; Moniruzzaman, M.; Yusup, S.; Welton, T., Ionic liquids assisted processing of renewable resources for the fabrication of biodegradable composite materials. *Green Chemistry* **2017**, 19 (9), 2051-2075.
114. Thune, P.; Brolund, L., Short-and long-contact therapy using a new dithranol formulation in individually adjusted dosages in the management of psoriasis. *Acta dermato-venereologica. Supplementum* **1992**, 172, 28-29.
115. Lazzarini, P. A.; Pacella, R. E.; Armstrong, D. G.; Van Netten, J. J., Diabetes-related lower-extremity complications are a leading cause of the global burden of disability. *Diabetic Medicine* **2018**, 35 (9), 1297-1299.
116. Armstrong, D. G.; Boulton, A. J. M.; Bus, S. A., Diabetic foot ulcers and their recurrence. *New England Journal of Medicine* **2017**, 376 (24), 2367-2375.

117. Vivas, A.; Escandon, J.; Lebrun, E.; Choudhary, S.; Tang, J.; Kirsner, R. S., New therapies for treatment of diabetic foot ulcers: a review of current clinical trials. *Surgical technology international* **2010**, *20*, 83-96.
118. Benavente-Garcia, O.; Castillo, J., Update on uses and properties of citrus flavonoids: new findings in anticancer, cardiovascular, and anti-inflammatory activity. *J. Agric. Food. Chem.* **2008**, *56* (15), 6185-6205.
119. Parker, A. V.; Williams, R. N.; Paterson, C. A., The effect of sodium citrate on the stimulation of polymorphonuclear leukocytes. *Invest Ophthalmol Vis Sci* **1985**, *26* (9), 1257-61.
120. Pfister, R. R.; Nicolario, M. L.; Paterson, C. A., Sodium citrate reduces the incidence of corneal ulcerations and perforations in extreme alkali-burned eyes--acetylcysteine and ascorbate have no favorable effect. *Invest Ophthalmol Vis Sci* **1981**, *21* (3), 486-90.
121. Su, W.; Li, Z.; Li, Y.; Lin, M.; Yao, L.; Liu, Y.; He, Z.; Wu, C.; Liang, D., Doxycycline Enhances the Inhibitory Effects of Bevacizumab on Corneal Neovascularization and Prevents Its Side Effects. *Investigative Ophthalmology & Visual Science* **2011**, *52* (12), 9108-9115.
122. Takashina, Y.; Manabe, A.; Hasegawa, H.; Matsunaga, T.; Endo, S.; Ikari, A., Sodium Citrate Increases Expression and Flux of Mg<sup>2+</sup> Transport Carriers Mediated by Activation of MEK/ERK/c-Fos Pathway in Renal Tubular Epithelial Cells. *Nutrients* **2018**, *10* (10).
123. Yang, Y.; Pearson, R. M.; Lee, O.; Lee, C. W.; Chatterton, R. T.; Khan, S. A.; Hong, S., Drug Delivery: Dendron-Based Micelles for Topical Delivery of Endoxifen: A Potential Chemo-Preventive Medicine for Breast Cancer (Adv. Funct. Mater. 17/2014). *Adv. Funct. Mater.* **2014**, *24* (17), 2441-2441.
124. Šmejkalová, D.; Muthný, T.; Nešporová, K.; Hermannová, M.; Achbergerová, E.; Huerta-Angeles, G.; Svoboda, M.; Čepa, M.; Machalová, V.; Luptáková, D.; Velebný, V., Hyaluronan polymeric micelles for topical drug delivery. *Carbohydr. Polym.* **2017**, *156*, 86-96.
125. Roesken, F.; Uhl, E.; Curri, S. B.; Menger, M. D.; Messmer, K., Acceleration of wound healing by topical drug delivery via liposomes. *Langenbeck's archives of surgery* **2000**, *385* (1), 42-49.
126. Agarwal, R.; Iezhitsu, I.; Agarwal, P.; Abdul Nasir, N. A.; Razali, N.; Alyautdin, R.; Ismail, N. M., Liposomes in topical ophthalmic drug delivery: an update. *Drug delivery* **2016**, *23* (4), 1075-1091.
127. Wu, X.; Guy, R. H., Applications of nanoparticles in topical drug delivery and in cosmetics. *Journal of Drug Delivery Science and Technology* **2009**, *19* (6), 371-384.



128. Moddaresi, M.; Brown, M. B.; Zhao, Y.; Tamburic, S.; Jones, S. A., The role of vehicle–nanoparticle interactions in topical drug delivery. *Int. J. Pharm.* **2010**, *400* (1-2), 176-182.
129. Lee, H.; Xu, G.; Kharaghani, D.; Nishino, M.; Song, K. H.; Lee, J. S.; Kim, I. S., Electrospun tri-layered zein/PVP-GO/zein nanofiber mats for providing biphasic drug release profiles. *Int. J. Pharm.* **2017**, *531* (1), 101-107.
130. Karki, S.; Kim, H.; Na, S.-J.; Shin, D.; Jo, K.; Lee, J., Thin films as an emerging platform for drug delivery. *Asian journal of pharmaceutical sciences* **2016**, *11* (5), 559-574.
131. Hu, X.; Liu, S.; Zhou, G.; Huang, Y.; Xie, Z.; Jing, X., Electrospinning of polymeric nanofibers for drug delivery applications. *J. Controlled Release* **2014**, *185*, 12-21.
132. Zhang, H.; Mittal, G., Biodegradable protein-based films from plant resources: A review. *Environmental Progress & Sustainable Energy* **2010**, *29* (2), 203-220.
133. Bealer, E. J.; Kavetsky, K.; Dutko, S.; Lofland, S.; Hu, X., Protein and polysaccharide-based magnetic composite materials for medical applications. *Int. J. Mol. Sci.* **2020**, *21* (1), 186.
134. DeFrates, K.; Markiewicz, T.; Gallo, P.; Rack, A.; Weyhmler, A.; Jarmusik, B.; Hu, X., Protein polymer-based nanoparticles: fabrication and medical applications. *Int. J. Mol. Sci.* **2018**, *19* (6), 1717.
135. Torculas, M.; Medina, J.; Xue, W.; Hu, X., Protein-based bioelectronics. *ACS Biomaterials Science & Engineering* **2016**, *2* (8), 1211-1223.
136. Jao, D.; Xue, Y.; Medina, J.; Hu, X., Protein-based drug-delivery materials. *Materials* **2017**, *10* (5), 517.
137. DeFrates, K. G.; Moore, R.; Borgesi, J.; Lin, G.; Mulderig, T.; Beachley, V.; Hu, X., Protein-Based Fiber Materials in Medicine: A Review. *Nanomaterials* **2018**, *8* (7).
138. Bealer, E. J.; Onissema-Karimu, S.; Rivera-Galletti, A.; Francis, M.; Wilkowski, J.; Salas-de la Cruz, D.; Hu, X., Protein–Polysaccharide Composite Materials: Fabrication and Applications. *Polymers* **2020**, *12* (2), 464.
139. Selling, G. W.; Sessa, D. J.; Palmquist, D. E., Effect of water and tri (ethylene) glycol on the rheological properties of zein. *Polymer* **2004**, *45* (12), 4249-4255.
140. Wang, Y.; Filho, F. L.; Geil, P.; Padua, G. W., Effects of processing on the structure of zein/oleic acid films investigated by X-ray diffraction. *Macromolecular bioscience* **2005**, *5* (12), 1200-1208.

141. Dong, J.; Sun, Q.; Wang, J.-Y., Basic study of corn protein, zein, as a biomaterial in tissue engineering, surface morphology and biocompatibility. *Biomaterials* **2004**, *25* (19), 4691-4697.
142. Liu, X.; Sun, Q.; Wang, H.; Zhang, L.; Wang, J.-Y., Microspheres of corn protein, zein, for an ivermectin drug delivery system. *Biomaterials* **2005**, *26* (1), 109-115.
143. Zeng, M.; Huang, Y.; Lu, L.; Fan, L.; Mangavel, C.; Lourdin, D., Mechanical Properties of Thermo-moulded Biofilms in Relation to Proteins/Starch Interactions. *Food Biophysics* **2011**, *6* (1), 49-57.
144. Luecha, J.; Sozer, N.; Kokini, J., Synthesis and properties of corn zein/montmorillonite nanocomposite films. *Journal of Materials Science* **2010**, *45* (13), 3529-3537.
145. Rouf, T.; Schmidt, G.; Kokini, J., Zein-Laponite nanocomposites with improved mechanical, thermal and barrier properties. *Journal of Materials Science* **2018**, *53* (10), 7387-7402.
146. Kimna, C.; Tamburaci, S.; Tihminlioglu, F., Novel zein-based multilayer wound dressing membranes with controlled release of gentamicin. *Journal of Biomedical Materials Research Part B: Applied Biomaterials* **2019**, *107* (6), 2057-2070.
147. Shi, X.; Zhou, W.; Ma, D.; Ma, Q.; Bridges, D.; Ma, Y.; Hu, A., Electrospinning of nanofibers and their applications for energy devices. *Journal of Nanomaterials* **2015**, *2015*.
148. Abdal-Hay, A.; Hamdy, A. S.; Lim, J. H., Facile preparation of titanium dioxide micro/nanofibers and tubular structures by air jet spinning. *Ceram. Int.* **2014**, *40* (10), 15403-15409.
149. Stojanovska, E.; Canbay, E.; Pampal, E. S.; Calisir, M. D.; Agma, O.; Polat, Y.; Simsek, R.; Gundogdu, N. A. S.; Akgul, Y.; Kilic, A., A review on non-electro nanofibre spinning techniques. *RSC Adv.* **2016**, *6* (87), 83783-83801.
150. Sinha-Ray, S.; Sinha-Ray, S.; Yarin, A. L.; Pourdeyhimi, B., Theoretical and experimental investigation of physical mechanisms responsible for polymer nanofiber formation in solution blowing. *Polymer* **2015**, *56*, 452-463.
151. Simone, E. A.; Dziubla, T. D.; Muzykantov, V. R., Polymeric carriers: role of geometry in drug delivery. *Expert opinion on drug delivery* **2008**, *5* (12), 1283-1300.
152. Tungprapa, S.; Jangchud, I.; Supaphol, P., Release characteristics of four model drugs from drug-loaded electrospun cellulose acetate fiber mats. *Polymer* **2007**, *48* (17), 5030-5041.



153. Hu, X.; Kaplan, D.; Cebe, P., Determining Beta-Sheet Crystallinity in Fibrous Proteins by Thermal Analysis and Infrared Spectroscopy. *Macromolecules* **2006**, *39* (18), 6161-6170.
154. Xue, Y.; Wang, F.; Torculas, M.; Lofland, S.; Hu, X., Formic Acid Regenerated Mori, Tussah, Eri, Thai, and Muga Silk Materials: Mechanism of Self-Assembly. *ACS Biomaterials Science & Engineering* **2019**, *5* (12), 6361-6373.
155. Wang, F.; Wu, H.; Venkataraman, V.; Hu, X., Silk fibroin-poly(lactic acid) biocomposites: Effect of protein-synthetic polymer interactions and miscibility on material properties and biological responses. *Materials Science & Engineering C* **2019**, *104*, 109890-109890.
156. Gillgren, T.; Barker, S. A.; Belton, P. S.; Georget, D. M. R.; Stading, M., Plasticization of Zein: A Thermomechanical, FTIR, and Dielectric Study. *Biomacromolecules* **2009**, *10* (5), 1135-1139.
157. Giri, A.; Makhal, A.; Ghosh, B.; Raychaudhuri, A. K.; Pal, S. K., Functionalization of manganite nanoparticles and their interaction with biologically relevant small ligands: Picosecond time-resolved FRET studies. *Nanoscale* **2010**, *2* (12), 2704-2709.
158. Müller-Goymann, C. C., Physicochemical characterization of colloidal drug delivery systems such as reverse micelles, vesicles, liquid crystals and nanoparticles for topical administration. *European journal of pharmaceutics and biopharmaceutics* **2004**, *58* (2), 343-356.
159. Ramakrishna, S.; Fujihara, K.; Teo, W.-E.; Yong, T.; Ma, Z.; Ramaseshan, R., Electrospun nanofibers: solving global issues. *Mater. Today* **2006**, *9* (3), 40-50.
160. Liu, Y.; Nguyen, A.; Allen, A.; Zoldan, J.; Huang, Y.; Chen, J. Y., Regenerated cellulose micro-nano fiber matrices for transdermal drug release. *Materials Science & Engineering C* **2017**, *74*, 485-492.
161. Medicinal Applications for Electrospun Nanofibers. *Electrospinning* **2012**, 217-236.
162. Goyal, R.; Macri, L. K.; Kaplan, H. M.; Kohn, J., Nanoparticles and nanofibers for topical drug delivery. *J. Controlled Release* **2016**, *240*, 77-92.
163. Prasopchai Tonglairoum, T. N. T. R. R. K. P. O., Fabrication of a novel scaffold of clotrimazole-microemulsion-containing nanofibers using an electrospinning process for oral candidiasis applications. *Colloids and Surfaces B: Biointerfaces* **2015**, *126*, 18-25.
164. Juejing Liu, F. O. D. X. F. X. F. W.-H. Z., A protein-functionalized microfiber/protein nanofiber Bi-layered air filter with synergistically enhanced filtration performance by a viable method. *Sep. Purif. Technol.* **2019**, *229*, 115837-115837.

165. Goh, Y.-F.; Shakir, I.; Hussain, R., Electrospun fibers for tissue engineering, drug delivery, and wound dressing. *Journal of Materials Science* **2013**, *48* (8), 3027-3054.
166. Tonglairoum, P.; Ngawhirunpat, T.; Rojanarata, T.; Kaomongkolgit, R.; Opanasopit, P., Fabrication of a novel scaffold of clotrimazole-microemulsion-containing nanofibers using an electrospinning process for oral candidiasis applications. *Colloids Surf. B* **2015**, *126*, 18-25.
167. Bambole, V.; Yakhmi, J. V., Chapter 14 - Tissue engineering: Use of electrospinning technique for recreating physiological functions. In *Nanobiomaterials in Soft Tissue Engineering*, Grumezescu, A. M., Ed. William Andrew Publishing: 2016; pp 387-455.
168. Kishimoto, Y.; Morikawa, H.; Yamanaka, S.; Tamada, Y., Electrospinning of silk fibroin from an aqueous solution at low concentration. *Mater. Sci. Eng. C* **2017**, *73*, 498-506.
169. Shamshina, J. L.; Zavgorodnya, O.; Bonner, J. R.; Gurau, G.; Di Nardo, T.; Rogers, R. D., "Practical" Electrospinning of Biopolymers in Ionic Liquids. *ChemSusChem* **2017**, *10* (1), 106-111.
170. Zhang, F.; Lu, Q.; Yue, X.; Zuo, B.; Qin, M.; Li, F.; Kaplan, D. L.; Zhang, X., Regeneration of high-quality silk fibroin fiber by wet spinning from CaCl<sub>2</sub>-formic acid solvent. *Acta Biomater.* **2015**, *12*, 139-145.
171. Pereira, R. F. P.; Brito-Pereira, R.; Goncalves, R.; Silva, M. P.; Costa, C. M.; Silva, M. M.; de Zea Bermudez, V.; Lanceros-Mendez, S., Silk Fibroin Separators: A Step Toward Lithium-Ion Batteries with Enhanced Sustainability. *ACS Appl Mater Interfaces* **2018**, *10* (6), 5385-5394.
172. Ying-ying, L. I.; Fang, W.; Qi-chun, L. I. U.; Dong-min, Z.; Xue, Z.; Qing-yu, M. A.; Zheng-gui, G. U., Research Progress in Silk Fibroin and Its Composite Materials. *Journal of Materials Engineering* **2018**, *46* (8), 14-26.
173. Xia, X.-X.; Xu, Q.; Hu, X.; Qin, G.; Kaplan, D. L., Tunable Self-Assembly of Genetically Engineered Silk-Elastin-like Protein Polymers. *Biomacromolecules* **2011**, *12* (11), 3844-3850.
174. Hines, D. J.; Kaplan, D. L., Characterization of Small Molecule Controlled Release From Silk Films. *Macromol. Chem. Phys.* **2013**, *214* (2), 280-294.
175. Goormaghtigh, E.; Cabiaux, V.; Ruyschaert, J. M., Secondary structure and dosage of soluble and membrane proteins by attenuated total reflection Fourier-transform infrared spectroscopy on hydrated films. *Eur. J. Biochem.* **1990**, *193* (2), 409-420.
176. Dong, A.; Huang, P.; Caughey, W. S., Protein secondary structures in water from second-derivative amide I infrared spectra. *Biochemistry* **1990**, *29* (13), 3303-3308.

177. Mouro, C.; Jung, C.; Bondon, A.; Simonneaux, G., Comparative Fourier transform infrared studies of the secondary structure and the CO heme ligand environment in cytochrome P-450cam and cytochrome P-420cam. *Biochemistry* **1997**, *36* (26), 8125-8134.
178. Tretinnikov, O. N.; Tamada, Y., Influence of casting temperature on the near-surface structure and wettability of cast silk fibroin films. *Langmuir* **2001**, *17* (23), 7406-7413.
179. Teramoto, H.; Miyazawa, M., Molecular orientation behavior of silk sericin film as revealed by ATR infrared spectroscopy. *Biomacromolecules* **2005**, *6* (4), 2049-2057.
180. Defrates, K.; Markiewicz, T.; Callaway, K.; Xue, Y.; Stanton, J.; Salas-de La Cruz, D.; Hu, X., Structure–property relationships of Thai silk–microcrystalline cellulose biocomposite materials fabricated from ionic liquid. *Int. J. Biol. Macromol.* **2017**, *104* (Pt A), 919-928.
181. Díez-Pascual, A. M.; Díez-Vicente, A. L., Development of linseed oil–TiO<sub>2</sub> green nanocomposites as antimicrobial coatings. *Journal of Materials Chemistry B* **2015**, *3* (21), 4458-4471.
182. Arakawa, T.; Ejima, D.; Tsumoto, K.; Obeyama, N.; Tanaka, Y.; Kita, Y.; Timasheff, S. N., Suppression of protein interactions by arginine: A proposed mechanism of the arginine effects. *Biophys. Chem.* **2007**, *127* (1), 1-8.
183. O'Neil, M. J.; Smith, A.; Heckelman, P. E.; Budavari, S., The merck index-An encyclopedia of chemicals, drugs, and biologicals. whitehouse station, NJ: Merck and Co. *Inc* **2001**, *767*, 4342.
184. Nagiah, N.; Murdock, C. J.; Bhattacharjee, M.; Nair, L.; Laurencin, C. T., Development of Tripolymeric Triaxial Electrospun Fibrous Matrices for Dual Drug Delivery Applications. *Scientific Reports* **2020**, *10* (1), 609-609.
185. Luciani-Giacobbe, L. C.; Lorenzutti, A. M.; Litterio, N. J.; Ramirez-Rigo, M. V.; Olivera, M. E., Anti-tuberculosis site-specific oral delivery system that enhances rifampicin bioavailability in a fixed-dose combination with isoniazid. *Drug Deliv Transl Res* **2021**, *11* (3), 894-908.
186. Kim, S. H.; Lee, K. M.; Lee, G. S.; Seong, J.-W.; Kang, T. J., Rifampicin alleviates atopic dermatitis-like response in vivo and in vitro. *Biomolecules & therapeutics* **2017**, *25* (6), 634.
187. Maley, A. M.; Arbiser, J. L., Gentian Violet: a 19th century drug re-emerges in the 21st century. *Experimental dermatology* **2013**, *22* (12), 775-780.
188. Loeffler, A. M., Uses of rifampin for infections other than tuberculosis. *The Pediatric infectious disease journal* **1999**, *18* (7), 631-632.

189. Shui, T.; Shi, C.; Jing, Z.; Yang, D.; Zhu, J., Case Report: Rifampicin-Induced Thrombocytopenia in a Patient with Borderline Lepromatous Leprosy. *Am J Trop Med Hyg* **2020**, *103* (4), 1441-1442.
190. Sousa, G.; Carreiro, A.; Duarte, P., Rifampicin-induced disseminated intravascular coagulation: An antibody-mediated side effect. *Pulmonology* **2021**, *27* (3), 269-272.
191. Su, Q.; Kuang, W.; Hao, W.; Liang, J.; Wu, L.; Tang, C.; Wang, Y.; Liu, T., Antituberculosis Drugs (Rifampicin and Isoniazid) Induce Liver Injury by Regulating NLRP3 Inflammasomes. *Mediators Inflamm* **2021**, *2021*, 8086253.